

1 Motivation

Supersymmetry is able to offer solutions to unexplained phenomena in astrophysics and can solve the shortcomings of the Standard Model of particle physics (see Section ??). Unfortunately, due to the unknown mechanism of supersymmetry breaking, the most general parametrisation of Supersymmetry introduces over 100 new parameters and thus opens up an incredibly large phenomenological space, leading to very different possible signatures at particle colliders. A variety of searches were hunting for SUSY during the Phase I run at the LHC in 2012. Proton-proton collision data from the CMS and ATLAS experiments were analysed with a strong focus on the search for SUSY in the strong production sector (e. g. [1–3]). As a consequence, wide regions of SUSY parameter space are already excluded and the search for SUSY in more "exotic" regions gains more and more attention. Typical SUSY scenarios that are not easily excluded by the general SUSY searches consist of so-called compressed spectra where two or more particles are nearly mass-degenerate. Such scenarios can have two very distinctive phenomenological properties. First, if mother and daughter particles in a two body decay are almost mass-degenerate, the remaining decay product can be very soft in p_T , making them very hard to detect. Second, the mother particle can be long-lived due to phase space suppression (see Section ??). Because of these two properties, scenarios with compressed spectra can be challenging to search for and are in general much weaker constrained.

In R-parity conserving Supersymmetry, compressed spectra can be realised if the lightest neutralino (χ_1^0) is almost mass-degenerate with the lightest chargino (χ_1^\pm). Such a mass-degeneracy naturally occurs in case of wino-like neutralinos and charginos, since the mass gap between W_3 and $W_{1/2}$ is fully determined by higher loop corrections (see Section ??). SUSY models with a wino-like lightest neutralino are especially interesting because they are able to explain the sources of the relic density FIXME []. While it is not possible to explain the full relic density with thermally produced neutralinos for $m_{\chi_1^0} \lesssim 2.9$ TeV [4], neutralinos can still be the dominant part if they are non-thermally produced via the decay of a long-lived particle such as a wino-like chargino [5].

At the LHC, there are several possible chargino production channels. Chargino pairs can be produced through a photon or a Z -boson exchange. The chargino then decays via a virtual W -boson to the lightest neutralino and a fermion pair (e. g. a pion). This process is illustrated in the Feynman diagram in Fig. 1.1. Other possible chargino pair

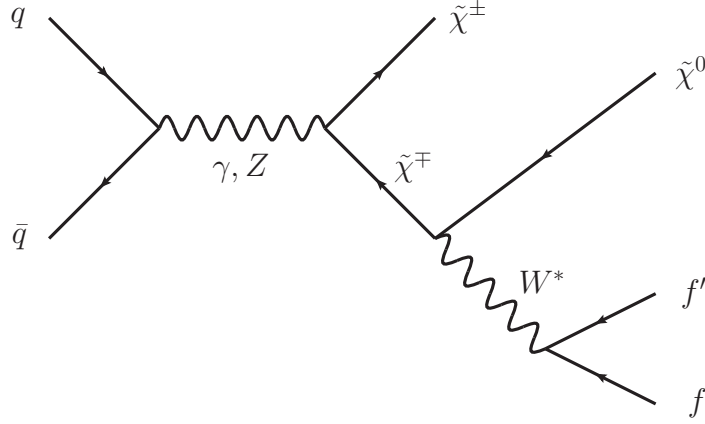


Figure 1.1: Feynman diagram of chargino pair production via gamma or Z -boson exchange and the subsequent decay via a virtual W -boson.

production channels include the exchange of a supersymmetric Higgs boson or a t-channel squark exchange (Fig. 1.2).

Apart from pair production, charginos can be produced via the chargino neutralino production channel. On tree-level, there exist two production mechanisms: the s-channel W -boson exchange and the t-channel squark exchange (Fig. 1.3).

Thus, the LHC offers the potential to search for charginos and due to its high centre-of-mass energy it is the first collider that can access SUSY models with charginos of several hundreds GeV.

Although supersymmetric models with nearly mass-degenerate $\tilde{\chi}_1^\pm$ and $\tilde{\chi}_1^0$ lead to exotic signatures with long lived charginos and soft decay products, existing SUSY searches at CMS can in principle be sensitive to these models. The exclusion power of existing SUSY searches can be assessed by interpreting their results in terms of the fraction of excluded parameter points in the phenomenological MSSM (see Section ?? for a detailed

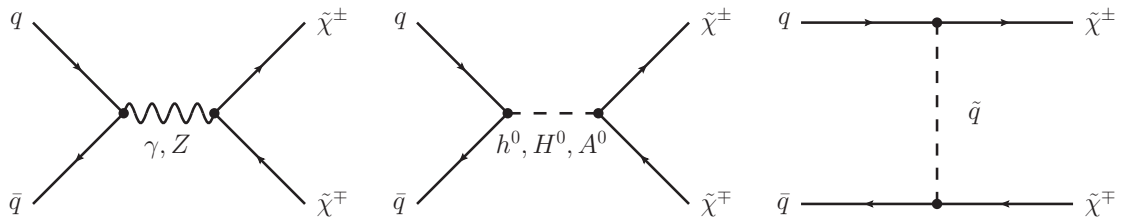


Figure 1.2: Main tree-level diagrams for chargino pair production.

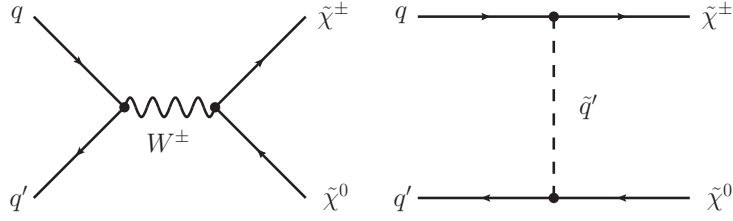


Figure 1.3: Main tree-level diagrams for chargino neutralino production.

introduction to the pMSSM). The results of such a study which has been performed in [6] are shown in Figure 1.4. It can be seen that general SUSY searches (blue area) are mostly sensitive to shorter chargino lifetimes ($c\tau \lesssim 10 \text{ cm}$)¹. Two existing searches, the search for long-lived charged particles [7] and the search for disappearing tracks [6] focus on long and intermediate chargino lifetimes respectively. These two searches (purple and red areas) are sensitive to chargino lifetimes of $\gtrsim 35 \text{ cm}$. Taken together, the existing searches exclude a large fraction of pMSSM points at different chargino lifetimes. However, there is a gap between the general SUSY searches and the search for disappearing tracks where none of the existing searches show a high sensitivity.

The here presented analysis aims at targeting this gap by focusing on charginos with intermediate lifetimes of $10 \text{ cm} \lesssim c\tau \lesssim 40 \text{ cm}$. The main idea is to make use of the variable dE/dx which can be very discriminating for massive particles such as charginos. The associated challenges and the general strategy of this analysis will be presented in the next section.

2 General search strategy

When searching for supersymmetric models with long-lived $\tilde{\chi}_1^\pm$, the strategy is of course highly dependent on the actual lifetime of the chargino. For long lifetimes, the chargino can reach the muon chambers and can be reconstructed as a muon even despite a longer time-of-flight [11]. For lower lifetimes, the chargino can already decay inside the detector (e.g. the tracker), and can hence not be reconstructed as a muon but leads to an isolated, potentially disappearing track in the tracker. The detector signatures of these two sce-

¹It should be mentioned, that the pMSSM interpretation relied on the use of fast simulation techniques which are not capable of simulating charginos with lifetimes $c\tau > 1 \text{ cm}$. It could therefore not be tested to which exact upper lifetime the searches combined in the blue area are sensitive to.

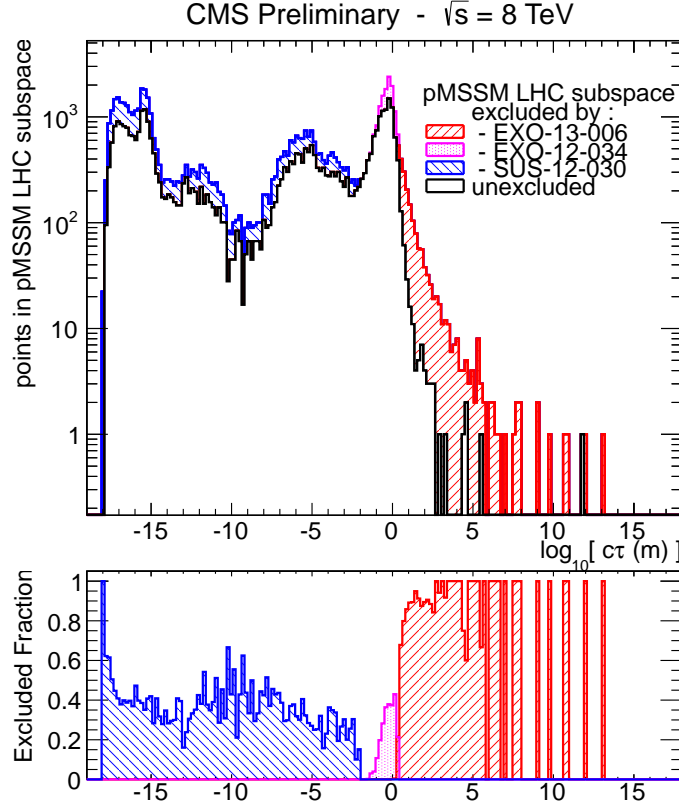


Figure 1.4: The number of excluded pMSSM points at 95% C.L. (upper part) and the fraction of excluded pMSSM points (bottom part) vs. the chargino lifetime for different CMS searches. Red area: the search for long-lived charged particles [7], Purple area: the search for disappearing tracks [6], Blue area: a collection of various general SUSY searches [8] The black line indicates the unexcluded pMSSM parameter points. The sampling of the parameter space points was done according to a prior probability density function which takes pre-LHC data and results from indirect SUSY searches into account (see [9] for further details). Taken from: [10].

narios are visualised in Fig. 2.1, where simulated chargino-chargino events are shown in a cross-sectional view of the CMS detector.

Since this analysis targets a search for Supersymmetry with charginos of lifetimes between $10 \text{ cm} \lesssim c\tau \lesssim 40 \text{ cm}$, the charginos decay rather early in the detector, even in the inner layers of the tracker. Thus, the signature of the chargino consists of an isolated track and the signatures of the decay products, i. e. of a neutralino and a fermion pair. In case of R-parity conservation the neutralino is stable and weakly interacting, thus traversing the detector without leaving any further signature. The missing transverse energy of the neutralino is balanced by the missing transverse energy of the second produced SUSY particle. This is either a neutralino or the decay products of the chargino in events with

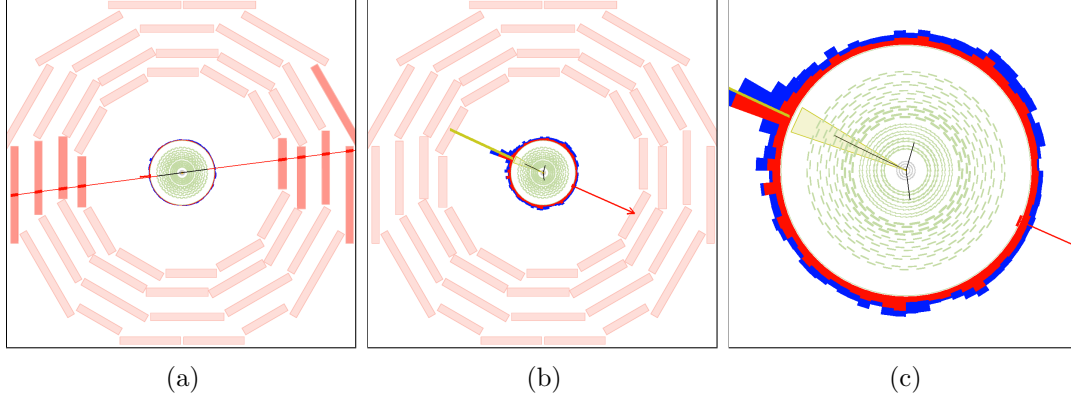


Figure 2.1: Visualisation of possible signatures of a chargino pair produced with a lifetime of $c\tau = 10$ m (a) and a lifetime of $c\tau = 0.5$ m (b and c). In the left picture, both charginos are reconstructed as muons, which can be seen in the energy deposition in the muon chambers (red boxes). In the middle picture both charginos are only visible as tracks in the tracker (black lines), where both trajectories end inside the silicon strip tracker, showing the decay point of the corresponding chargino. The right picture is a zoom of the picture in the middle. Here, only the cross-section of the tracker (green wavy lines for the strip and grey lines for the pixel) is displayed. The red arrow shows the missing transverse energy in the event. The red (blue) towers correspond to the energy deposition in the ECAL (HCAL).

chargino pairs.

The signature of the fermion pair can in principle be used to select chargino events. However, for mass-degenerate charginos, it can be very hard or even impossible to detect these fermions as will be explained in detail in the next paragraph.

First of all, the fermionic decay product (e.g. a pion) can hardly be reconstructed because it does not origin from the primary vertex. Secondly, it is very low in momentum because of the mass-degeneracy between $\tilde{\chi}_1^\pm$ and $\tilde{\chi}_1^0$. The typical momentum of a pion originating from a chargino to neutralino decay in the $\tilde{\chi}_1^\pm$ rest frame is of the order

$$p_\pi \sim \sqrt{m_{\tilde{\chi}_1^\pm} - m_{\tilde{\chi}_1^0} - m_\pi}.$$

For a mass gap between $\tilde{\chi}_1^\pm$ and $\tilde{\chi}_1^0$ of $\Delta m = 150$ MeV, the p_T distribution of the resulting pion peaks at ~ 100 MeV and ends at $p_T \sim 400$ MeV (Fig. 2.2).

If the transverse momentum of a particle is very low, the particle trajectory is much more bended compared to a particle with higher p_T (see Fig. 2.3 for illustration). Due to this bending, the track reconstruction efficiency of particles with a transverse momentum below 1 GeV decreases rapidly, reaching around 40% for isolated pions with a p_T of 100 MeV [12]. It is therefore impossible to rely on a reconstruction of the fermionic chargino decay

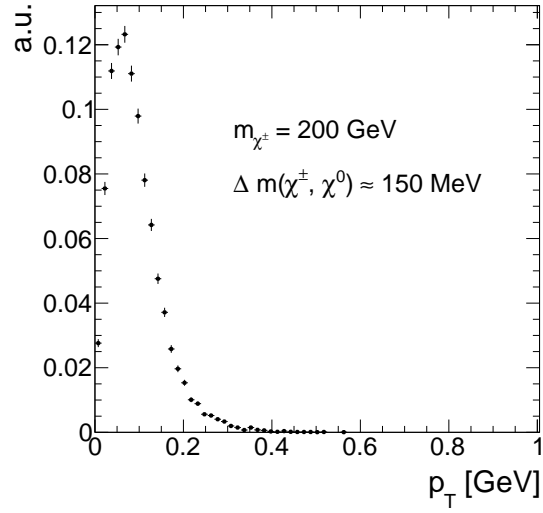


Figure 2.2: Transverse momentum distribution of pions coming from chargino decay into a neutralino with a mass gap of 150 MeV.

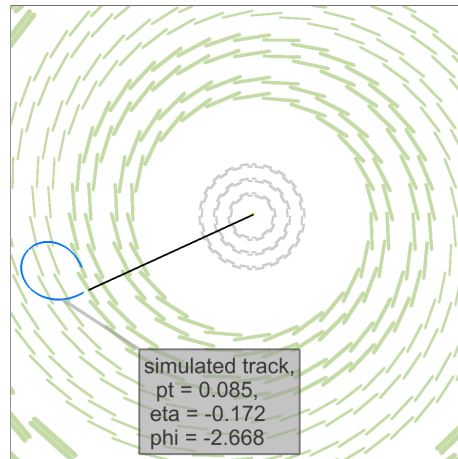


Figure 2.3: Cross-sectional view of the tracker (silicon strip (silicon pixel) tracker layers are illustrated with green (grey) lines) and a simulated chargino track (black line) decaying to a pion (bended blue line) with a p_T of ~ 85 MeV and a neutralino (not visible).

products in this analysis.

In summary, the signature of chargino events in mass-degenerate SUSY models consists only of a potentially disappearing- track. Such a signature is very difficult to detect, especially since CMS doesn't offer a dedicated track trigger so that triggering on the chargino track is impossible.

In order to search for such signatures, one therefore needs to trigger on other, less obvious properties of chargino events. This analysis takes advantage of higher order contributions to the Feynman diagrams shown in the previous sections (Figs. 1.2, 1.3), resulting in initial state radiation (ISR). If the initial quarks radiate a high p_T gluon, the resulting jet can be detected and can offer a possibility to search for events with nothing more than isolated tracks. Furthermore, the non-detection of the chargino's decay products plus a high p_T ISR jet lead to missing transverse energy (MET) in the event. Exploiting these two circumstances, it is possible to detect chargino-pair or chargino-neutralino events with the help of Jet+MET triggers.

Since Jet+MET triggers are not very specific for chargino events, it is important to identify further track properties that can be used to select chargino candidates. One distinctive property of charginos compared to SM particles is their high mass. Therefore, charginos can be identified by selecting high p_T tracks. Furthermore, the energy loss per path length (dE/dx) depends quadratically on the particle's mass for low velocities ($0.2 < \beta\gamma < 0.9$):

$$\left\langle \frac{dE}{dx} \right\rangle = K \frac{m^2}{p^2} + C$$

Therefore, dE/dx constitutes a very nice discriminating variable for massive particles like charginos against SM particles. The selection of chargino events in this analysis thus relies on the selection of isolated high p_T tracks with high dE/dx values.

If the chargino decays before it has crossed the full pixel and strip detector, the associated track is disappearing. For low lifetimes, the tracks can be very short and can have only a few hits in the detector. In order to reconstruct a particle's trajectory, a minimum of three hits are required since defining a helical path requires five parameters (see [12]). A specific challenge for this analysis is hence the combination of searching for short tracks and utilising the measurement of the energy deposition of the chargino. For very short tracks, eventually only passing the first couple of layers of the whole tracker system, the pixel tracker information becomes very important. Therefore, an accurate energy measurement in the pixel system is of great importance to this analysis. However, no other CMS analysis has used the energy information of the pixel tracker so far. This analysis thus requires a thorough study of the quality of the pixel energy calibration and, potentially, a recalibration in case the pixel energy calibration is not sufficient.

2.1 Comparison to existing searches

As already mentioned before, there are several analyses at CMS at $\sqrt{s} = 8$ TeV with 20 fb^{-1} data, that are sensitive to intermediate lifetime charginos, most notably the search for long-lived charged particles [7] and the search for disappearing tracks [6]. The here presented analysis aims at achieving an increase in sensitivity towards shorter lifetimes compared to the existing analyses in a twofold way. First, the selection is optimised for the inclusion of very short tracks. Second, the inclusion of the variable dE/dx is used to increase the search sensitivity compared to [6].

In [7], a minimum number of eight hits were required for every track, whereas [6] required a minimum of seven hits. This can be very inefficient for shorter lifetimes, where most of the charginos already decay shortly after the pixel tracker. In Fig. 2.4 (left), the normalised distribution of the number of measurements (N_{hits}) of chargino tracks is shown. It can be seen, that N_{hits} peaks at the minimal possible value needed for track reconstruction of $N_{\text{hits}} = 3$ for lower lifetimes. For higher lifetimes ($c\tau = 50 \text{ cm}$) the distribution shifts to higher values with a second peak at $N_{\text{hits}} \sim 17$. However, a notable fraction of $\sim 40\%$ of chargino tracks still has a number of measurements of $N_{\text{hits}} < 8$.

It should be also mentioned, that the track reconstruction efficiency is sufficient for short chargino tracks, such that a loosening of the N_{hits} requirement is expected to be really improving the signal acceptance. The track reconstruction efficiency for different chargino decay points is depicted in Fig. 2.4 (right). For very short tracks ($N_{\text{hits}} = 3$) the efficiency is still around 20%.

Additionally, the search for disappearing tracks which targets models with charginos decaying inside the tracker did not make use of the high energy deposition of heavy particles. Although this variable was indeed used in the search for long-lived charged particles, this search was not optimised for intermediate lifetimes (e. g. no explicit muon veto on the selected tracks was required). Thus, it shows less sensitivity compared to the disappearing track search in the lifetime region between $35 \text{ cm} \lesssim c\tau \lesssim 100 \text{ cm}$ (see Fig. 1.4).

To conclude, the general search strategy of the here presented analysis is to unite the strategies of [7] and [6] and to lower the strong selection on the number of hits in these analyses in order to get an optimised selection for lifetimes around $10 \text{ cm} \lesssim c\tau \lesssim 40 \text{ cm}$.

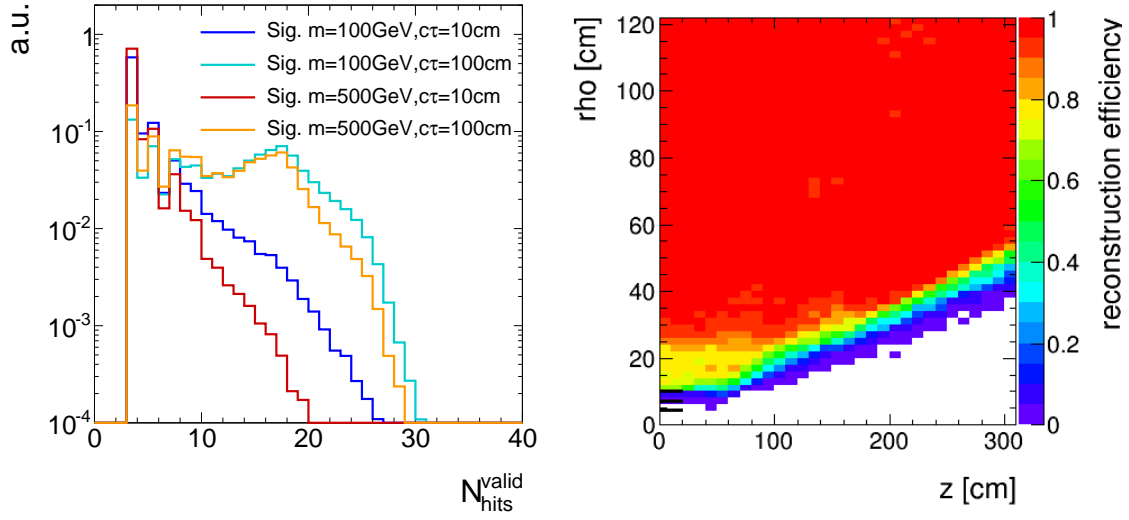


Figure 2.4: Left: Number of measurements in the tracker system N_{hits} for four different signal lifetimes. The low lifetime samples are rapidly falling and peaking at the lowest number of possible measurements of three. For a lifetime of $c\tau = 50$ cm, a second peak at ~ 17 hits appears corresponding to the number of measurements when crossing all pixel barrel (3) and strip inner and outer barrel (6 from stereo and 8 from normal) layers. Right: Probability to reconstruct a track (z) in dependency of the chargino's decay point (x and y). More information on the generation of the simulated signal samples can be found in Section 4.2

3 Improved dE/dx measurement of short tracks

The CMS tracker system does not only allow for the precise measurement of particle's tracks and primary and secondary vertices but also the measurement of a particle's energy loss within the tracker material. This is done by the detection of the number of electrons produced by the ionisation of the particle during its passage through the silicon tracker. A detailed introduction to the CMS tracker system and the energy measurement can be found in Section ??.

It was already pointed out that the inclusion of the pixel energy measurements can increase the sensitivity when searching for short tracks. While the silicon strip detector has already been calibrated as part of the search for long-lived charged particles [7], no

offline calibration has been done for the pixel silicon tracker so far. To increase the discrimination power of dE/dx for short tracks, such a calibration procedure was therefore conducted within this PHD thesis.

3.1 Ionisation loss of charged particles

The mean energy loss per path length of particles travelling through a layer of material can be described with the Bethe formula [13]:

$$\langle \frac{dE}{dx} \rangle = K z^2 \frac{Z}{A} \frac{1}{\beta^2} \left[\frac{1}{2} \ln \frac{2m_e c^2 \beta^2 \gamma^2 T_{\max}}{I^2} - \beta^2 - \frac{\delta(\beta\gamma)}{2} \right].$$

It is valid if the main energy loss originates from ionisation effects, i. e. in a region between $0.1 \lesssim \beta\gamma \lesssim 1000$. It is a function of the atomic number (Z) and the atomic mass (A) of the absorber. The mean excitation energy (I) for silicon is 173 eV [14]. T_{\max} represents the maximum energy transfer in a single collision. The relevant particle's properties are the velocity (β), the Lorentz factor (γ) and the charge (z) of the incident particle. The density correction $\delta(\beta\gamma)$ reduces the mean energy loss at high energies because of polarisation effects of the material. The constant factor K is $4\pi N_A r_e^2 m_e^2 c^2$ with N_A being the Avogadro's number.

Even if widely used, the mean energy loss is a quantity which is “ill-defined experimentally and is not useful for describing energy loss by single particles” [15]. The problem is caused by the underlying probability distribution of one single dE/dx measurement (this will be named $\Delta E/\Delta x$ throughout the following sections), which can be parametrised by a Landau distribution [16]

$$p(x) = \frac{1}{\pi} \int_0^\infty e^{-t \log t - xt} \sin(\pi t) dt.$$

The Landau distribution has no free parameters. Its most probable value is around 0.222. However, it is possible to introduce artificially a different most probable value and a width with $x \rightarrow \frac{x - \text{MPV}}{\sigma} - 0.222$. The Landau distribution is a highly asymmetric distribution with a long tail towards the right end (see Fig. 3.1). Theoretically it extends to infinite energies, however in nature the maximal deposited energy is of course limited by the particle's full energy. The mean and the variance of a Landau distribution are not defined. Because of its strong asymmetry, measurements of $\langle dE/dx \rangle$ with only a few single measurements are easily biased towards high values, making the mean energy loss described by the Bethe formula a problematic and unstable concept.

A much better observable is the most probable value (MPV): the maximum of the Landau distribution. The MPV is much more stable compared to the mean and is not as easily biased towards higher dE/dx values. The most probable energy loss of a charged

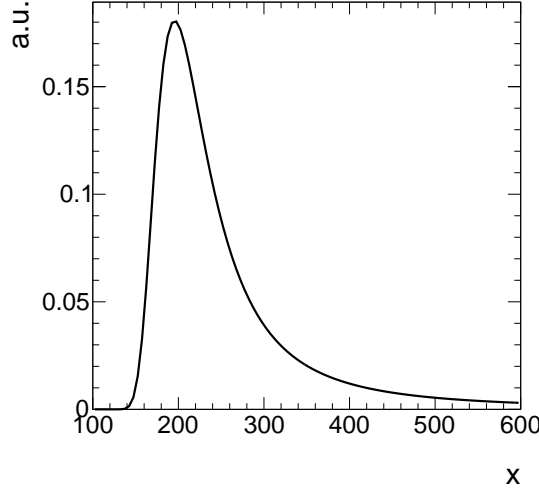


Figure 3.1: Illustration of the shape of a Landau distribution. Parameters were chosen as $\mu = 200$ and $\sigma = 20$.

particle, Δ_p , is defined by the Landau-Vavilov-Bichsel equation [17]:

$$\Delta_p = \xi \left[\ln \frac{2mc^2\beta^2\gamma^2}{I} + \ln \frac{\xi}{I} + j - \beta^2 - \delta(\beta\gamma) \right], \quad (3.1)$$

with $\xi = (K/Z)\langle Z/A \rangle(x/\beta^2)$. The thickness of the absorber x appears explicitly in the Landau-Vavilov-Bichsel equation making the most probable energy loss per path length Δ_p/dx logarithmically dependent on x . A comparison between the Bethe mean energy loss $\langle dE/dx \rangle$ and the most probable energy loss Δ_p/dx is shown in Fig. 3.2.

However, it is difficult to determine the most probable value for tracks with only ~ 15 energy measurements available. Large fluctuations can still lead to a bias towards higher value of the most probable dE/dx .

Several "estimators" exist that suppress a potential bias towards the high end without introducing a bias towards lower values [18]. One of the estimators, also used in the next chapter, is the harmonic-2 estimator

$$I_{h2} = \left(\frac{1}{N} \sum_{i=1}^N (\Delta E / \Delta x)_i^2 \right)^{-1/2}, \quad (3.2)$$

where $\Delta E / \Delta x$ corresponds to one measurement in one tracker module. The harmonic mean of all N measurements to the power of two is the estimated most probable dE/dx .

SM particles such as pions and muons are minimally ionising in silicon for $\beta\gamma \sim 3 -$

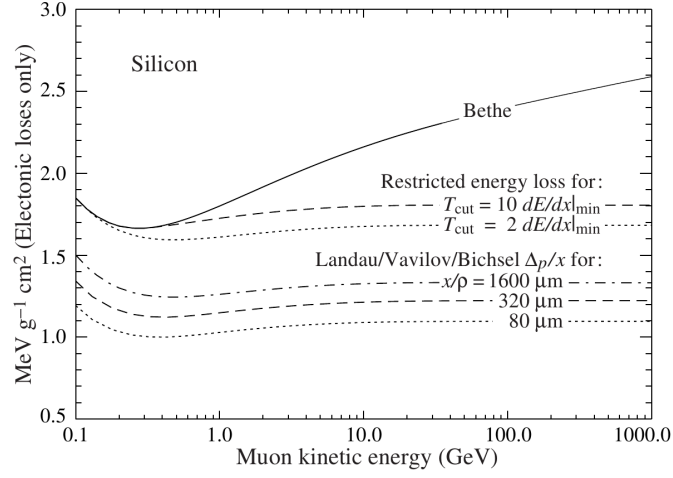


Figure 3.2: Comparison between the Bethe mean energy loss, restricted energy loss and the most probable energy loss described by the Landau-Vavilov-Bichsel function for muons for different values of absorber thickness. Taken from [15].

4 (see Fig. 3.3). For higher momenta the deposited energies increase again reaching a plateau at around $\beta\gamma \sim 100$. However, new heavy charged particles would mainly be unrelativistic because of their high mass and would therefore deposit much higher energies in the detector. This makes dE/dx a very well discriminating variable. Thus, the energy loss per path length can be used to discriminate between SM particles and new heavy charged particles, which are usually unrelativistic because of their high mass.

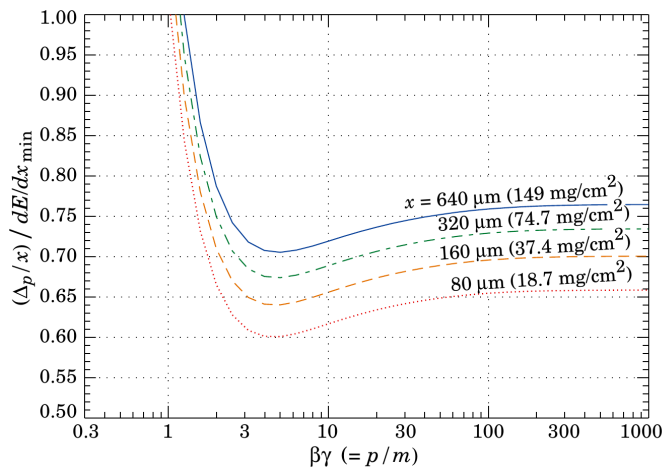


Figure 3.3: Most probable energy loss in silicon, scaled to the mean loss of a minimally ionising particle ($388 \text{ eV}/\mu\text{m}$) for different absorber thicknesses. Taken from [15].

3.2 Energy calibration of the silicon pixel tracker

During Run I in 2012, the pixel silicon detector was continuously subjected to an energy calibration, a so-called gain calibration [19]. Every pixel was calibrated to the same response, so that the whole pixel tracker should have been well inter-calibrated. Unfortunately, due to various reasons, such as the imperfect constancy of the reference signal, or radiation and temperature induced changes, the energy calibration could not ensure a fully calibrated pixel tracker. This imperfection of the gain calibration can be seen in Fig. 3.4, where the sum of the harmonic-2 estimator for all tracks $\sum_{\text{all trks}} I_{h2}$ over the full data-taking period in 2012 is shown. Four different steps can be spotted. The first and the third steps correspond to changes in the settings of the tracker due to irradiation. The second and fourth step are induced by associated adjustments in the online gain calibration. Unfortunately, although the gain calibration was adjusted (even with some delay), it was not able to ensure a constant energy response of the pixel tracker over time. The variations of the dE/dx measurement over time of around 15% is too large to use dE/dx without a further calibration.

The following sections explain the method of the gain calibration of the pixel silicon tracker which was conducted for this analysis. It is splitted into a section about the inter-calibration of gain and the absolute calibration of gain) Detailed technical information about the pixel tracker can be found in Section ??.

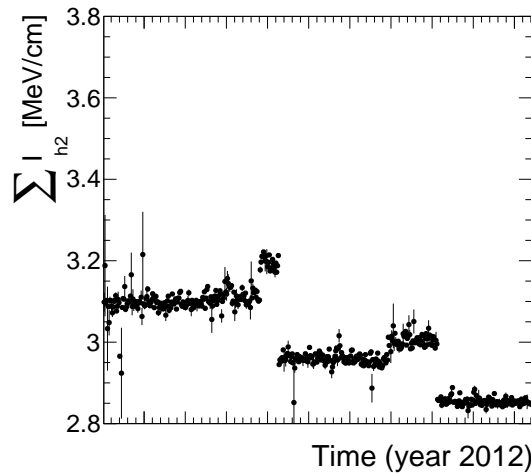


Figure 3.4: Sum of all track's dE/dx (harmonic-2 estimator) over the full year 2012. Only pixel hits are taken into account. Every data point corresponds to one run.

Inter-calibration of gain

The main goal of the gain calibration is to get a uniform response in the ionisation energy loss dE/dx over the full data taking period in 2012. To also ensure a uniform response of all modules within one time step, an additional inter-calibration on module level was carried out. The inter-calibration can in principle be done on various levels: the highest granularity would be a calibration on pixel level, followed by a calibration on read-out-chip (ROC) level and then on module-level. Lower granularities in descending order are rings (modules with same z-position) and finally layers (3 layers in the barrel and 4 disks in the endcap). It was checked that all pixels and all ROCs (on one module) are well inter-calibrated, such that the inter-calibration was finally done module-wise.

The gain calibration of the pixel silicon tracker has been carried out with the help of minimally ionising particles (MIPs). MIPs in this context are not defined as particles depositing a minimum amount of energy, but more generally a small amount of energy. This denotes all particles located at the plateau of the dE/dx distribution vs. momentum (see Fig. 3.3). This approach ensures that all particles deposit similar amount of energy so that the variation due to different momenta is minimised. MIPs are selected by a momentum selection of $p > 2$ GeV. Additionally, only tracks with at least eight hits and a $\chi^2/\text{n.d.o.f.} < 3$ are used to ensure a high-quality track reconstruction. A sample containing around 50 million “minimum bias” events is used for calibration. The “minimum bias” sample was specifically recorded for tracker calibration purposes. Its distinctive property is that neither an online nor offline selection was applied.

For every module in the pixel tracker (there are 1440 modules in total), a distribution of the energy loss per path length $\Delta E/\Delta x$ is built. The measurement of $\Delta E/\Delta x$ is done in ADC counts per mm. ADC counts are a measure for the deposited charge after digitisation. Figure 3.5 shows an example distribution for one module. The underlying Landau distribution can be nicely seen. To extract the MPV for every module a fit to the core distribution is performed. The fit is done with a Landau convoluted with a Gaussian function to be closer to the experimentally observed energy spectrum. This also increases the fit performance and the stability of the fit. The path length Δx is calculated with

$$\Delta x = d_{\text{module}_i} \cdot \cos(\phi_{\text{track}}),$$

where d_{module_i} is the thickness of module i and ϕ_{track} is the relative angle of the particle’s trajectory to the normal axis of the module. With the measured MPV extracted from the fit, an inter-calibration factor is calculated for every module

$$c_{\text{inter}} = \frac{\text{MPV}_{\text{target}} [\text{ADC/mm}]}{\text{MPV} [\text{ADC/mm}]} = \frac{300 \cdot 265 \text{ ADC/mm}}{\text{MPV} [\text{ADC/mm}]}.$$

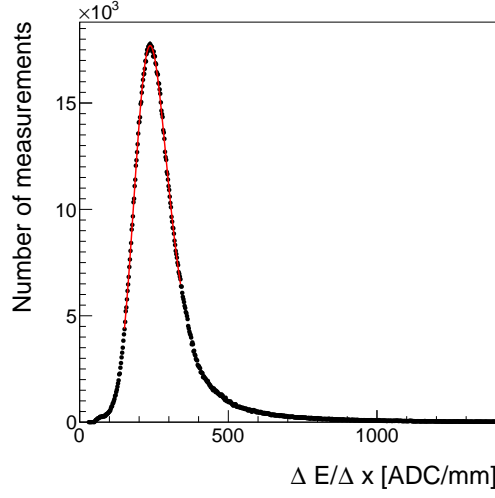


Figure 3.5: An example of the $\Delta E/\Delta x$ distribution measured in ADC count per mm for one module of the CMS pixel tracker. A Landau convoluted with a Gaussian is fitted to the core of the distribution in an iterative procedure.

The factor $300 \cdot 265$ ADC/mm is in principal an arbitrary number since the final response is adjusted by the absolute gain calibration described in the next section. However, it was chosen such that it corresponds approximately to the most probable energy deposition of a MIP. The calibration factor can then be used to scale every single measurement in a module to a calibrated $\Delta E/\Delta x$ measurement

$$\frac{\Delta E}{\Delta x}_{\text{calibrated}} = c_{\text{inter}} \cdot \frac{\Delta E}{\Delta x}_{\text{uncalibrated}}$$

The determination of the calibration factor needs to be done for every of the five time steps, shown in Fig. 3.4 independently, in order to get rid of the time dependency. The result of the inter-calibration can be seen in Fig. 3.6. The variation over time was indeed eradicated, resulting in a maximal time variation of less than $\sim 1\%$.

Additionally, the same procedure is carried out for a corresponding simulated data sample to ensure the inter-calibration of the pixel modules on all simulated samples.

Absolute calibration of gain

As a final step, the targeted MPV being $\text{MPV}_{\text{target}} = 300 \cdot 265$ ADC/mm needs to be translated to a meaningful physical quantity given in physical units (e. g. MeV/cm). That means, that the charge measurement in ADC counts needs to be converted to the real energy release of a particle. The relation between ΔE in ADC counts and the energy loss

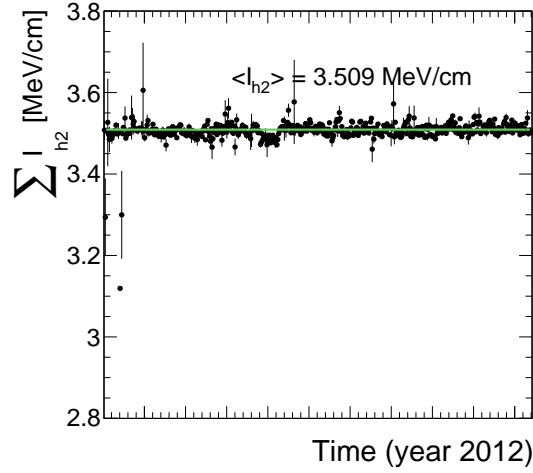


Figure 3.6: Sum of all track's dE/dx (harmonic-2 estimator) over the full year 2012 after applying the calibration factors, resulting in an average dE/dx of 3.51 MeV/cm. Only pixel hits are taken into account. Every data point corresponds to one run.

in eV is given by

$$\Delta E [\text{eV}] = c_{\text{inter}} \cdot \Delta E [\text{ADC}] \cdot \frac{N_e}{\text{ADC}} \cdot 3.61 \text{ eV},$$

where N_e/ADC is the number of electrons which correspond to one ADC count and 3.61 eV is the mean energy needed to create one electron-hole pair in silicon at -10°C . Such an absolute gain calibration can be done with the help of several methods (all explained in [18]). The absolute calibration of the silicon pixel tracker can rely on the already conducted absolute calibration of the silicon strip detector. In [18], the absolute gain calibration was done with the help of the most probable energy release per path length of muons, theoretically described by the Landau-Vavilov-Bichsel formula in Eq. 3.1. To calibrate the pixel tracker to the correct energy loss per path length it is therefore sufficient to determine one calibration factor to relate the average dE/dx of all tracks in the pixel tracker as shown in Fig. 3.6 to the average measured dE/dx in the strip tracker, shown in Fig. 3.7 by

$$c_{\text{absolute}} = \frac{dE/dx_{\text{strip}}}{dE/dx_{\text{pixel}}} = \frac{3.303}{3.509} = 0.941.$$

This factor is then applied on top of c_{inter} for all pixel modules.

Finally, an absolute calibration factor needs to be determined for the simulated samples, where the simulated pixel tracker is calibrated to the average dE/dx of the silicon strip measured in data.

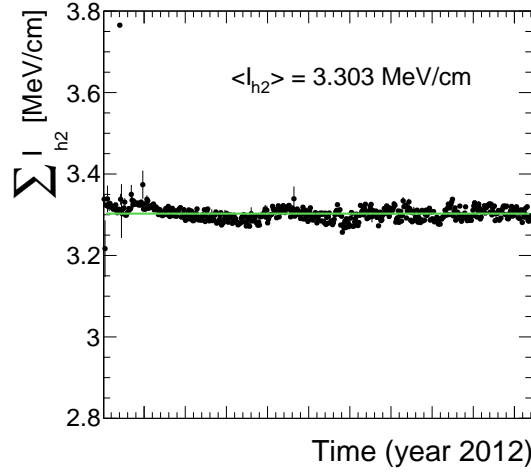


Figure 3.7: Sum of all track's dE/dx (harmonic-2 estimator) measured in the silicon strip detector over the full year 2012. The average most probable dE/dx is $I_{h2} = 3.303$ MeV/cm. Every data point corresponds to one run.

3.3 Discrimination of highly-ionising particles

As mentioned before, it is difficult to find a robust estimator for the MPV of the Landau distribution, if only a few single measurements of $\Delta E/\Delta x$ are available. The harmonic-2 estimator I_{h2} was already introduced in Section 3.1 in Eq. 3.2. It is known to be a robust estimator not easily biased by large fluctuation in $\Delta E/\Delta x$ because of the suppression by a factor of two.

However, it was shown in [18] that a better discrimination between SM particles and possible new heavy particles can be achieved when using likelihood techniques, i.e. determining the probability that the set of all $\Delta E/\Delta x$ belonging to one track is actually compatible with the hypothetical probability distribution of a MIP.

Testing that a measured sample has been drawn from a specific distribution is known as the Smirnov-Cramér-von Mises test [20, 21], which is deduced from the integral of the squared difference of the measured distribution $P_N(x)$ to the hypothesis distribution $P(x)$

$$I_s = \int_{-\infty}^{\infty} [P_N(x) - P(x)]^2 dP(x)$$

leading to a test statistics of

$$I_s = \frac{3}{N} \cdot \left(\frac{1}{12N} + \sum_{i=1}^N \left[P_i - \frac{2i-1}{2N} \right]^2 \right),$$

where N is the total number of energy measurements and P_i is the cumulative probability that a MIP would release a $\Delta E/\Delta x$ equal or smaller than the measured $\Delta E/\Delta x$ with all P_i are arranged in increasing order.

However, this test statistics is not sensitive to the sign of the difference between the measured and the theoretical distribution. It can therefore not distinguish between incompatibilities due to variations towards higher or lower energy deposits compared to the hypothesis distribution. Thus it is not suitable for the discrimination between MIPs and heavy new particles by dE/dx . A so-called Asymmetric Smirnov-Cramér-von Mises discriminator was developed in [18] which is only sensitive to incompatibilities to the MIP hypothesis towards higher energy depositions

$$I_{\text{as}} = \frac{3}{N} \cdot \left(\frac{1}{12N} + \sum_{i=1}^N \left[P_i \cdot \left(P_i - \frac{2i-1}{2N} \right)^2 \right] \right).$$

A value of I_{as} close to zero indicates good compatibility with the MIP hypothesis, whereas a value close to one indicates worse compatibility because of unexpectedly high energy losses.

The underlying probability P_i of the energy release for a given path length in the pixel tracker is extracted from the same “Minimum bias” sample used for the pixel energy calibration. In total 28 different templates each for a different given path length are created. In Fig. 3.8 the probability distribution template for the pixel tracker in data and simulation is shown. The corresponding templates for the energy release in the silicon strip detector were already built by [18].

A comparison between the energy release by MIPs (I_{as}) in data and simulation for good quality tracks with $p > 5 \text{ GeV}$ and $|\eta| < 2.1$ can be found in Fig. 3.9. dE/dx shows good agreement in data and simulation for $I_{\text{as}} < 0.1$. For larger values, I_{as} shows a larger decrease in simulation than in measured data. That’s the reason why a data-based approach for analyses exploiting dE/dx information is needed.

3.4 Discrimination improvements

The goal of including the pixel energy information is to increase the discrimination power of I_{as} between background and signal tracks, especially for shorter lifetimes. In Fig. 3.10, a comparison of the shapes of the energy release by MIPs and by signal tracks in simulation is shown (details about the simulated samples can be found in the next section Section 4.2). It can be seen, that the I_{as} distributions of all signal models show a larger tail towards $I_{\text{as}} = 1$, whereas the I_{as} of the background is rapidly falling. The I_{as} distribution is not only influenced by the velocity (β) of a particle but also by the number of hits of a track. The

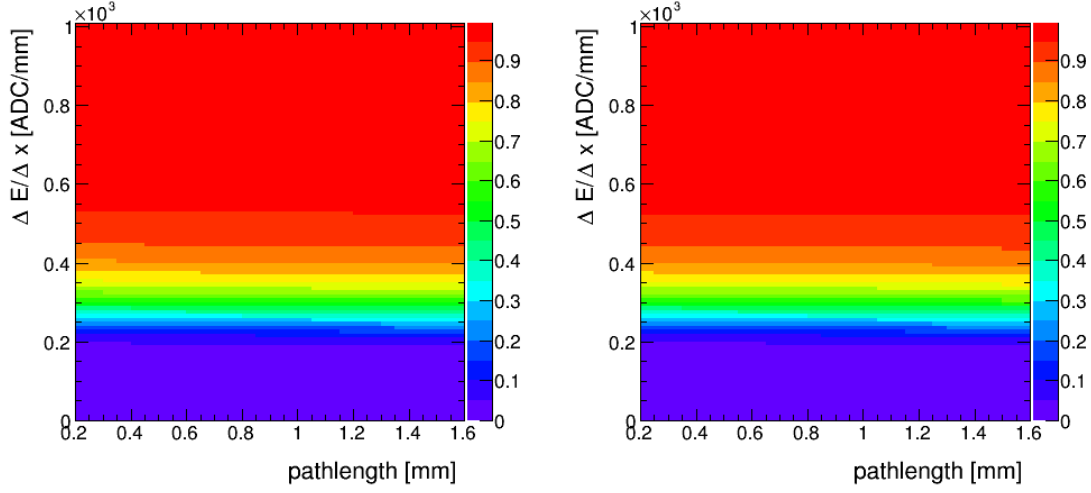


Figure 3.8: Cumulative probability for a MIP to release a $\Delta E/\Delta x$ (y-axis) vs. the path length (x-axis) in data (left) and simulation (right) for the pixel tracker based on the “Minimum bias” sample.

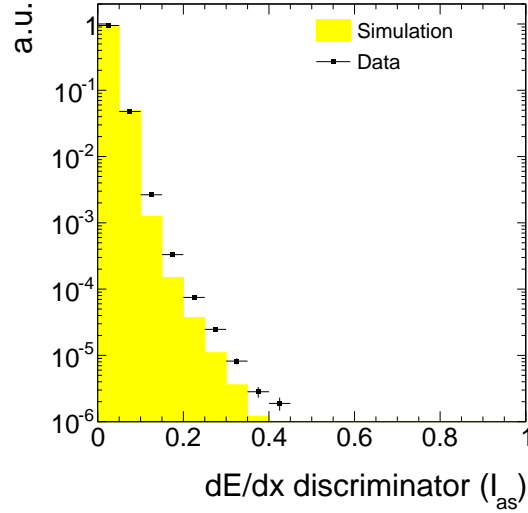


Figure 3.9: Normalised I_{as} distribution for MIPs from the minimum bias sample in data and simulation for good quality (high-purity as defined in [22] and minimum number of eight hits) tracks with $p > 5$ GeV and $|\eta| < 2.1$.

influence of the velocity can be easily seen in Eq. 3.1. This in turn results in a dependency of I_{as} on the mass of the incident particle. However, also for charginos with same mass, the velocity is higher in average for shorter lifetimes. This is caused by the fact, that for shorter lifetimes (e.g. $c\tau = 10$ cm), already a sizable fraction of the charginos decay before reaching the tracker system. The probability of reaching the detector increases for higher velocities because of the boost, which can be clearly seen at the survival probability

$$P(t) = e^{-\frac{t}{\gamma\tau}}. \quad (3.3)$$

This means that shorter lifetimes lead to higher average β which in turn lead to lower values of I_{as} .

The number of measurements in the tracker system defines the influence of single fluctuations in $\Delta E/\Delta x$ on the I_{as} discriminator, because of the long right tail of the Landau distribution, A low number of hits lead therefore to higher I_{as} values.

Thus, I_{as} for charginos with lower lifetimes are affected by two things: First, due to the smaller number of measurements the chargino tends to higher I_{as} values. Second, low lifetimes charginos have in average a higher velocity leading to lower I_{as} values. Both effects can be seen in Fig. 3.10 (right). The large tail for longer lifetimes is caused by the lower velocities, but the small surplus between 0.1 and 0.2 is caused by the smaller number of measurements for lower lifetimes.

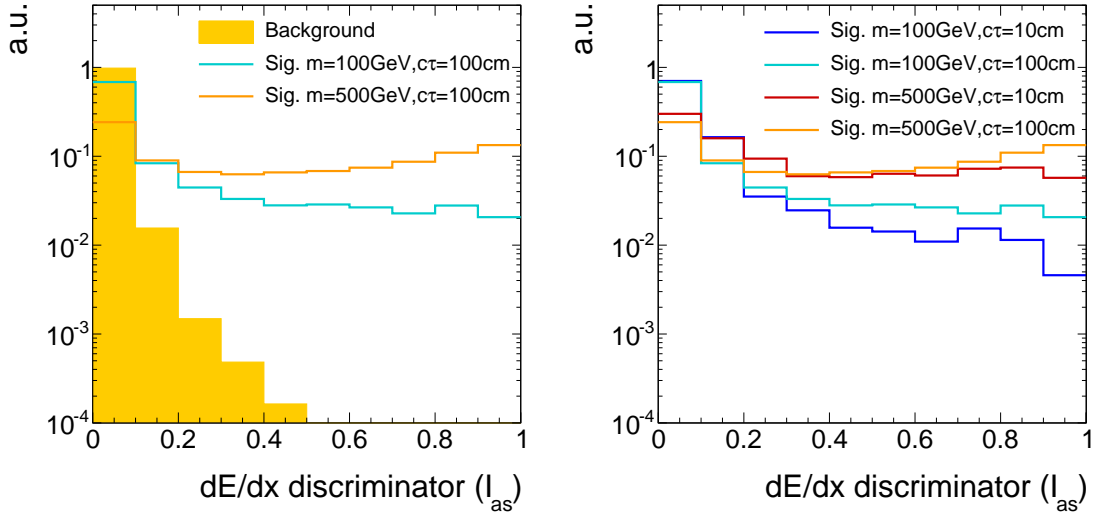


Figure 3.10: Normalised I_{as} distribution for simulated background and signal tracks (left) and for four different signal models (right) for high-purity tracks (as defined in [22]) with $p_T > 10$ GeV and $|\eta| < 2.1$. For the illustration of the background tracks' spectrum simulated $t\bar{t}$ +jets events are used (more information about this sample is given in Section 4).

Finally, the impact of the additional $\Delta E/\Delta x$ information from the pixel tracker on the selection efficiency of signal and background tracks is quantified. Figure 3.11 shows the signal selection efficiency against the background selection efficiency for different selection cuts in I_{as} , once including the pixel information and once without it. The background selection efficiency is estimated with simulated W +jets events but was additionally checked on simulated $t\bar{t}$ +jets and QCD-multijet events (further information about the simulated

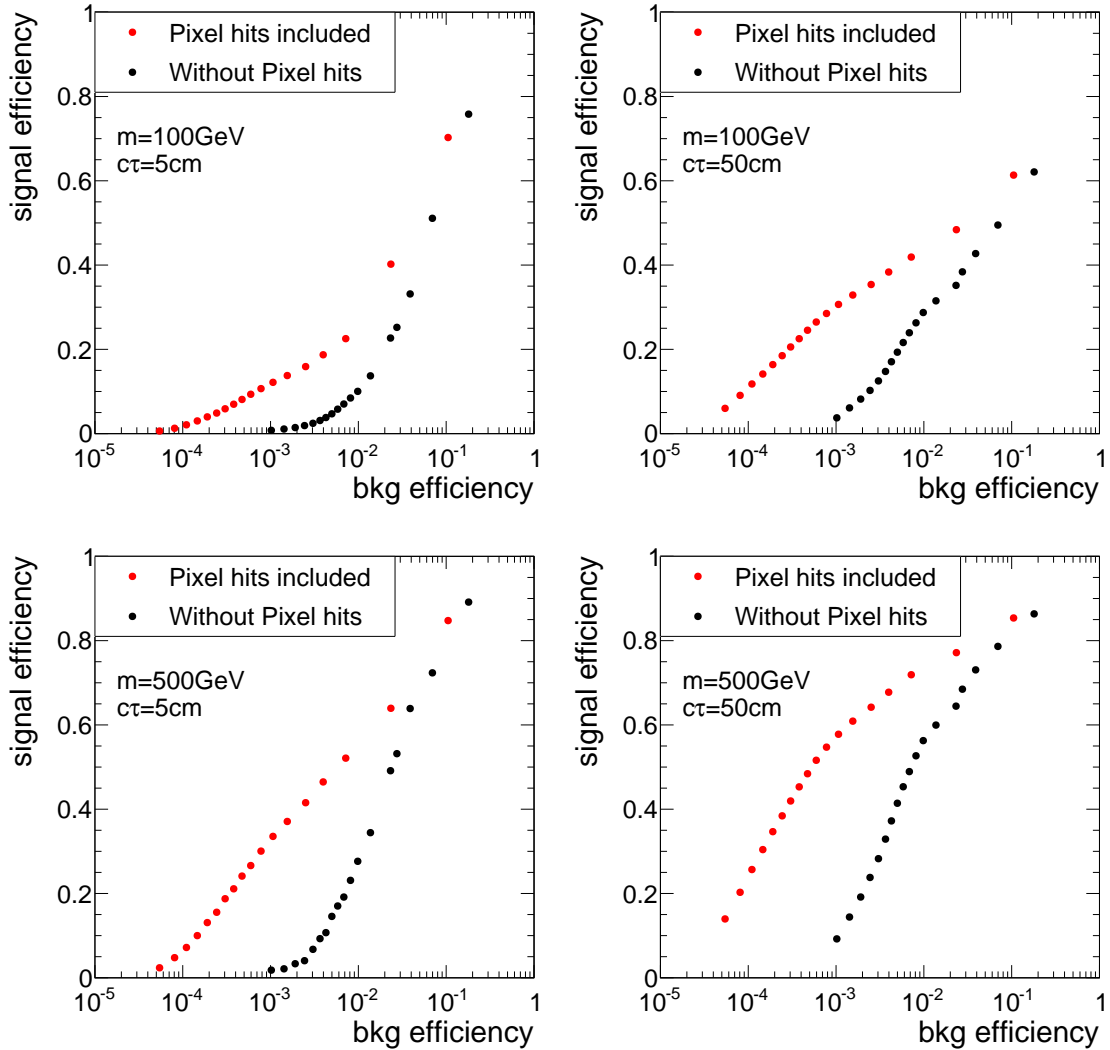


Figure 3.11: Signal selection efficiency vs. background selection efficiency with (red) and without (black) pixel information. Each point correspond to one selection cut in I_{as} . The figure is based on a simulated W + jets sample and a simulated signal sample with chargino-chargino production, both subject to a selection of good quality tracks with $p_T > 10$ GeV.

samples can be found in the next section). No significant difference between these processes in the background selection efficiency was observed.

The signal selection efficiency and the background suppression depend on the mass and the lifetime of the charginos. The discrimination power of I_{as} is much better for higher masses as expected.

It can be seen that the inclusion of the pixel information increases the background suppression for a given signal efficiency throughout the investigated signal models. This background suppression improvement is most pronounced for very tight cuts on I_{as} (up to a factor of 20) and still considerable for looser selections with signal efficiencies of around 40% (factor of 10).

4 Simulated samples

In order to design the search and to study background and signal characteristics, this analysis relies on simulated SM and SUSY datasets. An extensive introduction to the techniques and tools required for the simulation of SM and beyond SM processes can be found in Section ??.

The following two sections present an overview of the SM (Section 4.1) and SUSY samples (Section 4.2) used in this search. All samples are reweighted to match the measured distribution of primary vertices in data.

4.1 Standard Model background samples

To investigate the sources of background, various simulated SM samples are used. Since this analysis aims at making use of dE/dx , a special data format of the simulated samples, the so-called RECO format, is required. Unfortunately, not all SM processes are available in this specific format making it impossible to compare the total number of events in simulation and real data. This, however, does not constitute a serious problem since this analysis will finally use data-based background estimation methods. The simulated SM datasets can still be used to compare the shapes of important distributions in simulation and data.¹

In Table 4.1 all available SM samples used in this analysis are listed. Due to the size

¹For example, the simulated $Z \rightarrow \nu\bar{\nu} + \text{jets}$ sample that can contribute to the background of this search via fake tracks is not available in RECO format. However, as the shape of important observables of fake tracks is independent of the underlying process, this background can be studied with a simulated $W + \text{jets}$ sample.

Table 4.1: Available Standard Model background samples containing $\Delta E/\Delta x$ information that are used for background estimation studies.

Process	Cross section [pb]	$\mathcal{O}_{\text{calculation}}$
$W + \text{jets}$	36703.2	NNLO [23]
$t\bar{t} + \text{jets}$	245.8	NNLO [24]
$Z \rightarrow \ell\bar{\ell} + \text{jets}$ ($\ell = e, \mu, \tau$)	3531.9	NNLO [23]
QCD ($50 \text{ GeV} < \hat{p}_T < 1400 \text{ GeV}$)	9374794.2	LO

of the samples (between 5 and 70 TB) a reduction needs to be done in order to limit the storage space requirements. This is achieved by selecting only events which contain at least one jet with a minimum transverse momentum of $p_T > 60 \text{ GeV}$.

In addition, further simulated samples not containing the energy information are used. These are needed to study the background inclusively in the variable dE/dx . They are listed in Table 4.2.

Table 4.2: Standard Model background samples without $\Delta E/\Delta x$ information.

Process	Cross section [pb]	$\mathcal{O}_{\text{calculation}}$
$W + \text{jets}$	36703.2	NNLO [23]
$Z \rightarrow \ell\bar{\ell} + \text{jets}$ ($\ell = e, \mu, \tau$)	3531.9	NNLO [23]

4.2 Signal samples

For the investigation of a possible SUSY signal, events containing either chargino pair production $q\bar{q} \rightarrow \tilde{\chi}_1^\pm \tilde{\chi}_1^\mp$ or chargino neutralino production $q\bar{q} \rightarrow \tilde{\chi}_1^\pm \tilde{\chi}_1^0$ are simulated. The simulation is done with the matrix-element event generator MADGRAPH [25]. The parton showering and hadronisation processes are then simulated with PYTHIA [26]. Finally, the interactions of the generator-level particles with the detector material are simulated with GEANT4 [27, 28].

Furthermore, a special treatment for long-lived particles is required. In order to get a correct detector simulation of the energy loss of long-lived particles that decay after the

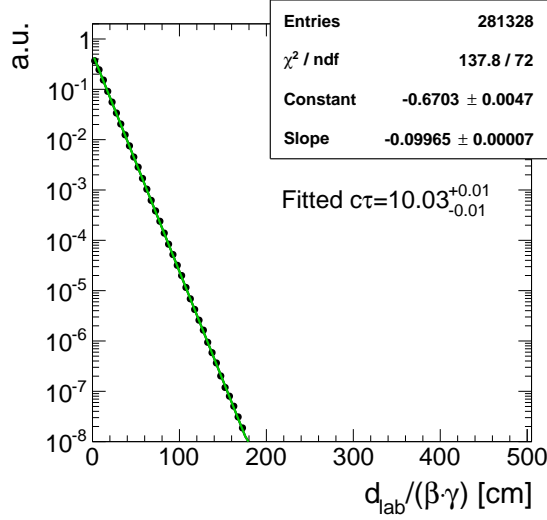


Figure 4.1: Normalised distribution of the proper individual lifetime $d_{\text{lab}}/(\beta\gamma)$ of all charginos contained in a signal sample with a generated lifetime of $c\tau^{\text{gen}} = 50$ cm reweighted to a lifetime of $c\tau^{\text{target}} = 10$ cm. Fitting an exponential curve $a \cdot \exp\left[\frac{1}{c\tau}ct_i\right]$ yields $c\tau = 1./\text{Slope} = 10$ cm.

beam pipe, the decay of the chargino cannot be simulated in the matrix-element generator but needs to be simulated within GEANT4.

To narrow down the required computing sources, the simulation is only done for a few lifetimes (1 cm, 5 cm, 10 cm, 50 cm, 100 cm, 1 000 cm and 10 000 cm). In order to scan in a high resolution over the lifetime space, other lifetimes are generated using lifetime reweighting. The weight for each event depends on the individual proper lifetime of the chargino and is given by

$$w = \prod_{i=1}^n \frac{\tau^{\text{gen}}}{\tau^{\text{target}}} \cdot \exp\left[t_i \cdot \left(\frac{1}{\tau^{\text{target}}} - \frac{1}{\tau^{\text{gen}}}\right)\right],$$

where n is the number of charginos in the event, τ^{gen} is the generated mean lifetime in the particle's rest frame and t_i is the individual proper lifetime of the chargino. The targeted mean lifetime is given by τ^{target} . A derivation of this formula can be found in Appendix ???. Using this reweighting procedure a good coverage of the lifetime space can be achieved with lifetimes of $c\tau = a \cdot 10^n$ for $n = 0, 1, 2, 3, 4$ and $a = [1, 9]$. Figure 4.1 shows the exponential distribution of the individual proper lifetime of the charginos after the reweighting of a simulated sample with $c\tau^{\text{gen}} = 50$ cm to a lifetime of $c\tau^{\text{target}} = 10$ cm. It can be seen that the reweighting procedure does indeed reproduce the targeted lifetime of 10 cm.

All samples are generated for different masses of the chargino, but always almost mass-

degenerate to the lightest neutralino. The mass gap between chargino and neutralino is set to 150 MeV. However, as this analysis does not make use of the decay products of the chargino and the lifetime is independently set within GEANT4, the mass gap does not play any role. Six different masses from 100 GeV to 600 GeV are simulated. This leads to a total number of 42 signal samples. In Table 4.3 cross sections at $\sqrt{s} = 8$ TeV for $\tilde{\chi}_1^\pm \tilde{\chi}_1^\mp$ and $\tilde{\chi}_1^\pm \tilde{\chi}_1^0$ production for wino-like charginos and neutralinos are listed [29, 30]. The cross section does not depend on the lifetime of the chargino.

Table 4.3: Simulated signal mass points with corresponding cross sections at NLO-NLL (NLO: next-to-leading order, NLL: next-to-leading logarithmic) accuracy for wino-like charginos.

$m_{\tilde{\chi}_1^\pm}$ [GeV]	$\sigma_{\tilde{\chi}_1^\pm \tilde{\chi}_1^\mp}$ [pb]	$\sigma_{\tilde{\chi}_1^0 \tilde{\chi}_1^\mp}$ [pb]
100	5.8234	11.5132
200	0.37924	0.77661
300	0.06751	0.14176
400	0.01751	0.03758
500	0.00553	0.01205
600	0.00196	0.00431

5 Event selection

5.1 Datasets and triggers

The analysis is performed on pp collision data recorded in the year 2012 at the CMS experiment for a centre-of-mass energy of $\sqrt{s} = 8$ TeV. In total an integrated luminosity of 19.7 fb^{-1} was recorded in 2012.

As outlined in Section 2, the detection of chargino tracks is a challenging task already on trigger level. Direct triggering of events containing chargino-like tracks is not possible because in 2012 there was no information about the tracking system available on trigger level L1. Furthermore, there is no intrinsic missing transverse energy in the event if the chargino decays inside the tracker. Therefore, this analysis uses initial state radiation for

the detection of chargino events. If ISR occurs, it is possible to trigger on a high- p_T jet ($p_T^{1.\text{jet}}$) and missing transverse energy (\cancel{E}_T).

For this purpose, several triggers are utilised in this analysis. An event is selected, if at least one of the three triggers in Table 5.1 fired.

Table 5.1: \cancel{E}_T and $\cancel{E}_T + \text{jet}$ triggers used in this analysis together with the corresponding recorded integrated luminosity during the time when they were in place.

Trigger	Luminosity [fb^{-1}]
HLTMonoCentralPFJet80_PFMETnoMu95_NHEF0p95	5.3
HLTMonoCentralPFJet80_PFMETnoMu105_NHEF0p95	14.4
HLT_MET120_HBHENoiseCleaned	19.7

The HLTMonoCentralPFJet80_PFMETnoMu95_NHEF0p95 and HLTMonoCentralPFJet80_PFMETnoMu105_NHEF0p95 triggers both rely on the L1 ETM40 trigger which requires the missing energy to be larger than 40 GeV. On HLT level, they further require at least one particle-flow jet with $p_T > 80$ GeV and a missing transverse momentum (not taking into account the p_T of muons) to be larger than 95 GeV or 105 GeV respectively. Finally, the energy release by neutral hadrons must not be larger than 95% for all jets in the event. The HLTMonoCentralPFJet80_PFMETnoMu95_NHEF0p95 trigger was active during Run A and Run B in 2012 data taking, whereas HLTMonoCentralPFJet80_PFMETnoMu105_NHEF0p95 was in place during Run C and Run D in 2012.

The HLT_MET120_HBHENoiseCleaned trigger is based on the two L1 triggers ETM40 and ETM36 that are combined by a logical OR. On HLT level, the trigger requires that the missing energy measured in the calorimeter is larger than 120 GeV. The HBHENoise-filter reduces background from electronic noise in the HCAL.

The events that were selected by the described triggers are available in the MET datasets listed in Table 5.2. Again, because of the size of the datasets (~ 150 TB in total), a reduction of the size is achieved by selecting only events where one of the used triggers fired and that contain at least one jet with a minimum p_T of 50 GeV.

5.2 Selection of signal candidate events

In order to suppress events originating from Standard Model processes such as QCD-multijet events, $W + \text{jets}$, etc., a selection for signal-like tracks is applied. The analysis

Table 5.2: MET data samples used in the search with the contained integrated luminosity.

Dataset	Luminosity [fb^{-1}]
/MET/Run2012A-22Jan2013-v1/RECO	0.876
/MET/Run2012B-22Jan2013-v1/RECO	4.412
/MET/Run2012C-22Jan2013-v1/RECO	7.055
/METParked/Run2012D-22Jan2013-v1/RECO	7.354

selection closely follows the selection required in [31, 32]. It relies on event-based and track-based variables as described in the following two sections.

5.2.1 Event-based selection

First a selection on the quality of the vertex is applied in order to suppress cosmic events and noise from the beam halo. This selection includes requirements on the position of the vertex with respect to the beam axes and the number of degrees of freedom of the vertex which is strongly correlated to the number of tracks originating from the vertex [33]:

- ❖ The vertex must have at least four degrees of freedom: vtx with ≥ 4 d.o.f.
- ❖ The position of the vertex along the beam line must be within 24 cm with respect to the nominal interaction point: $|dz| \leq 24$ cm.
- ❖ The position in the transverse direction must be within 2 cm with respect to the nominal interaction point: $|d0| \leq 2$ cm.

After these selection cuts are applied the remaining events are subjected to a further pre-selection.

To maximise the signal acceptance, the trigger related selection cuts are chosen as close as possible to the trigger thresholds (see Section 5.1). In Fig. 5.1, the distributions of \cancel{E}_T and the transverse momentum of the leading jet, $p_T^{1,\text{jet}}$, are shown for different signal models. Only jets with $|\eta| < 2.4$ that fulfil the following further criteria are taken into account:

- Charged hadron energy fraction CHF > 0.2
- Charged electromagnetic energy fraction CEF < 0.5

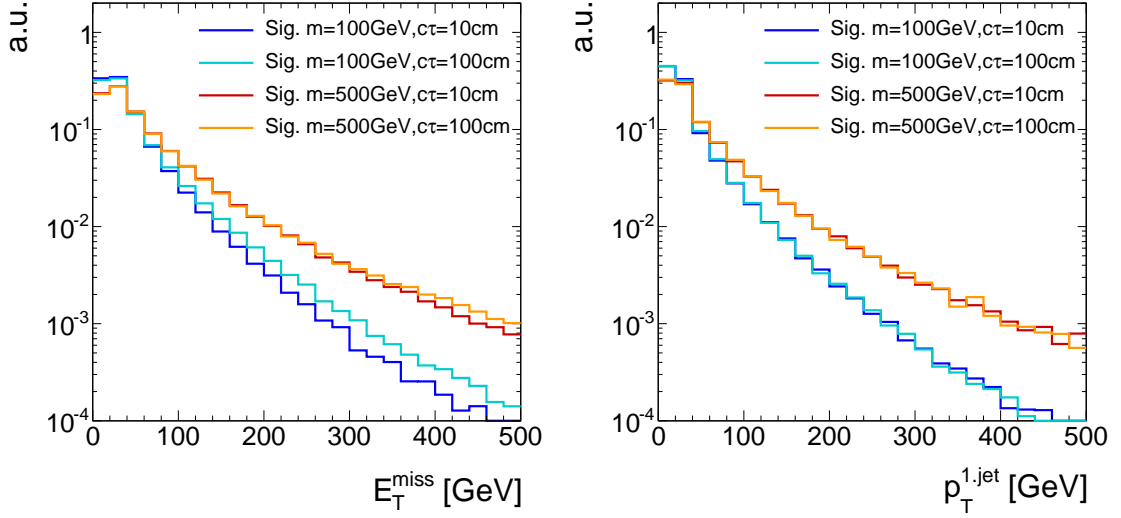


Figure 5.1: Normalised distributions of the missing transverse momentum (left) and the transverse momentum of the leading jet (right) for four different signal models.

- Neutral hadron energy fraction $\text{NHF} < 0.7$
- Neutral electromagnetic energy fraction $\text{NEF} < 0.7$.

These additional jet quality criteria ensure that noise from cosmic and beam halo muons and high- p_T photons and electrons is suppressed [34].

The trigger efficiency as a function of \cancel{E}_T and $p_T^{1,\text{jet}}$ was determined within [35] with a single-muon reference sample. The trigger paths become fully efficient for $p_T^{1,\text{jet}} \gtrsim 110$ GeV and $\cancel{E}_T \gtrsim 220$ GeV [34]. However, it can be seen in Fig. 5.1 that for a selection of $\cancel{E}_T > 220$ GeV more than 99% of the signal events are rejected.

In order to achieve a reasonable signal acceptance, this search imposes a trigger selection closer to the intrinsic trigger thresholds. The trigger requirements are as follows:

- ❖ There is at least one jet within $|\eta| < 2.4$ with transverse momentum larger than 110 GeV which fulfils the above mentioned jet noise cleaning criteria: $p_T^{1,\text{jet}} > 110$ GeV.
- ❖ The missing transverse momentum must be larger than 100 GeV: $\cancel{E}_T > 100$ GeV

These requirements result in a trigger efficiency of 100% in the variable $p_T^{1,\text{jet}}$ and $\sim 20\%$ in the variable \cancel{E}_T at the cut thresholds [34].

Because of the huge cross section, QCD-multijet events are frequently produced at the LHC. Due to jet energy mismeasurements, they can also contribute to data samples recorded with MET triggers. Therefore, special requirements are enforced in order to

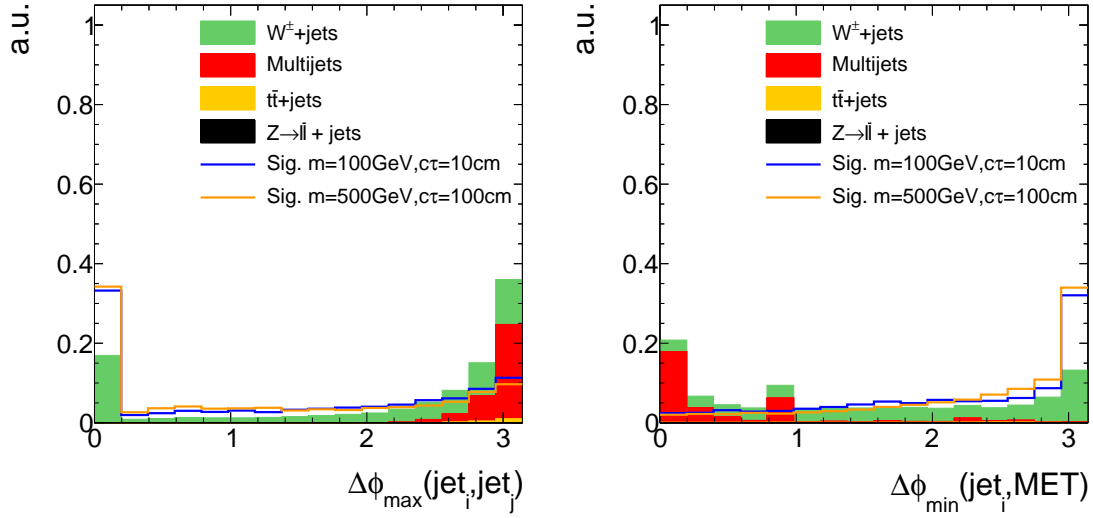


Figure 5.2: Maximum $\Delta\phi$ between any of two jets (left) and the minimum $\Delta\phi$ between the \cancel{E}_T vector and any of the two leading jets (right) normalised to unit area after the trigger selection. Only jets with $p_T > 20$ GeV and $|\eta| < 4.5$ are considered.

suppress events emerging from strong production processes. QCD-multijet events can be characterised by topologies where two jets are almost back-to back. Additionally, in QCD-multijet events the missing energy is usually aligned with one of the leading jets in the event. Figure 5.2 shows the maximum $\Delta\phi$ of any of two jets and the minimum $\Delta\phi$ between the \cancel{E}_T vector and any of the two leading jets for the SM background and two different signal datasets.

Therefore the following two requirements are sufficient to suppress QCD-multijet events efficiently:

- ❖ $\Delta\phi$ between any of two jets (with $p_T > 20$ GeV and $|\eta| < 4.5$) in the event must be smaller than 2.5.
- ❖ $\Delta\phi$ between any of the two leading jets (with $p_T > 20$ GeV and $|\eta| < 4.5$) and the \cancel{E}_T must be larger than 0.5.

5.2.2 Candidate track selection

After the reduction of background processes with event-based variables, a track-based selection is carried out. To get an optimised selection for possible chargino tracks several signal track characteristics are exploited.

First, a selection of high quality tracks is enforced:

- ❖ The track must be of “high purity” as defined in [22].
- ❖ The track is required to have no missing middle or inner hits: $N_{\text{miss}}^{\text{middle/inner}} = 0$
- ❖ The radial and longitudinal distance of the track to the primary vertex must be small: $|d0| < 0.02 \text{ cm}$, $|dz| < 0.5 \text{ cm}$.

In Figs. 5.3 and 5.4, the power of the latter two quality selection cuts is shown.

Furthermore, a first kinematic preselection is applied:

- ❖ Only tracks in the central region are considered : $|\eta| < 2.1$.
- ❖ Only tracks with a minimum transverse momentum of 20 GeV are considered: $p_T > 20 \text{ GeV}$.

In order to suppress background tracks emerging from SM processes, an electron, muon and tau veto is applied. This rejects tracks that are close to a reconstructed electron, muon or tau. Additionally, the candidate track must not be close to a jet ($p_T > 20 \text{ GeV}$ and $|\eta| < 4.5$).

Unfortunately, the lepton veto selection cuts lack efficiency in some of the detector directions. For example, the reconstruction of an electron easily fails in the direction of a dead ECAL cell. This reduces the discrimination power of the electron veto. For this

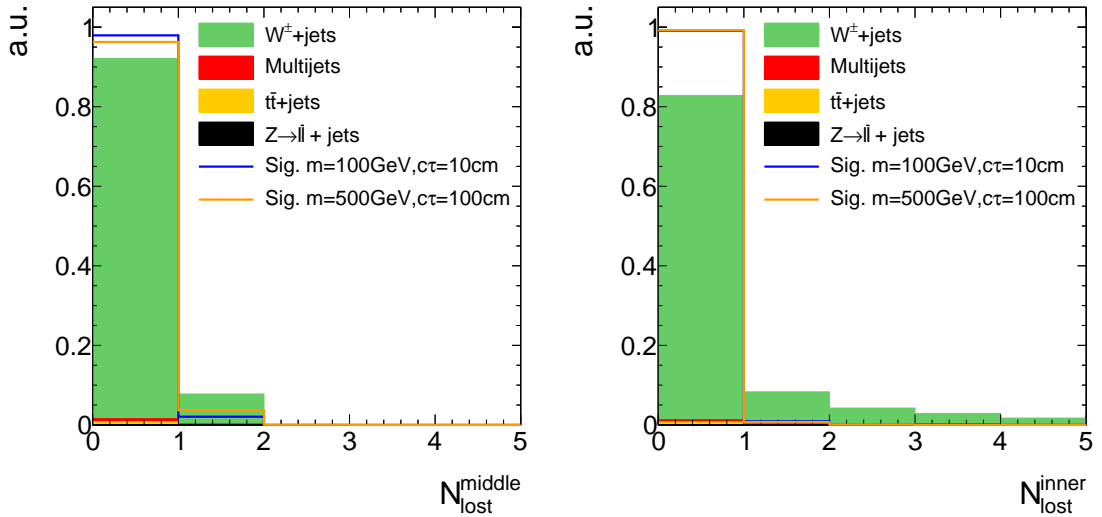


Figure 5.3: Number of missing middle (left) and inner (right) hits of background and signal tracks after trigger requirements and QCD suppression cuts.

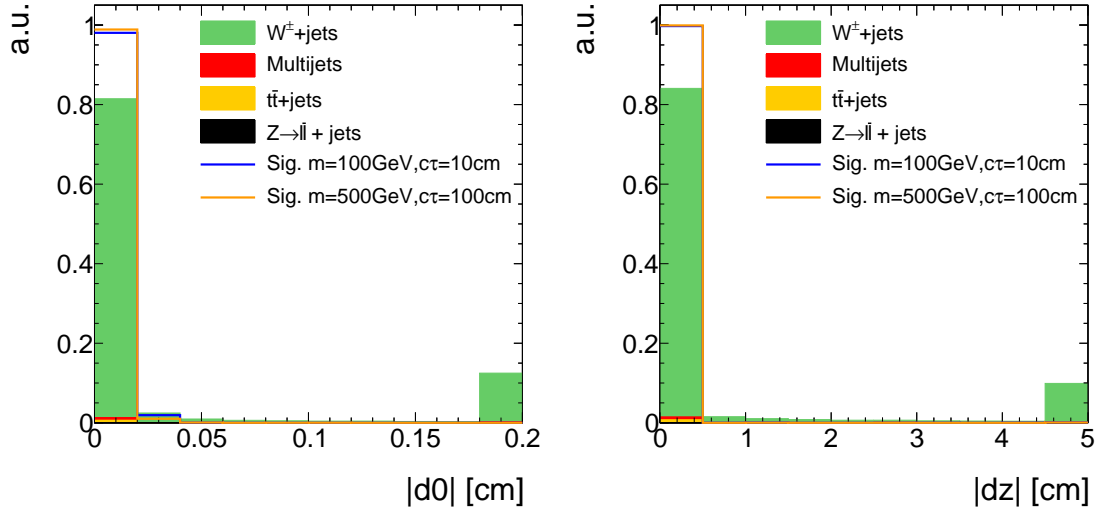


Figure 5.4: Absolute value of the radial (left) and longitudinal (right) distance between the track and the primary vertex after trigger requirements and multijet suppression cuts. Overflow entries are added to the last bin.

reason, tracks that point towards dead or noisy ECAL cells are rejected. A general list of dead and noisy ECAL cells is provided centrally at CMS. Further dead cells were identified within a study in [31,32] resulting in a total number of 1234 dead or noisy ECAL channels. These are illustrated in Fig. 5.5 showing a map of all ECAL channels not considered in the search.

Additionally, tracks that point towards intermodule gaps of ECAL cells or to the ECAL barrel endcap gap at $1.42 < |\eta| < 1.65$ are rejected. A list of the ECAL intermodule gaps, that is supplied centrally at CMS, is given in Table 5.3.

The muon reconstruction is less efficient for muons in detector regions with bad cathode strip chambers (CSC). These bad chambers are also identified centrally at CMS and their η and ϕ values are visualised in Fig. 5.6. Thus, also tracks pointing towards these regions within a distance of $\Delta R < 0.25$ are rejected.

To summarise, the candidate track must fulfil the following selection criteria:

- ❖ The track must not be within a cone of $\Delta R < 0.15$ to a reconstructed standalone, tracker or global muon with a transverse momentum larger than 10 GeV (see Section ?? for details on the different muon definitions).
- ❖ The track must not be within a cone of $\Delta R < 0.15$ to a reconstructed electron with a transverse momentum larger than 10 GeV (see Section ?? for details on the electron reconstruction).
- ❖ The track must not be within a cone of $\Delta R < 0.15$ to a reconstructed tau with

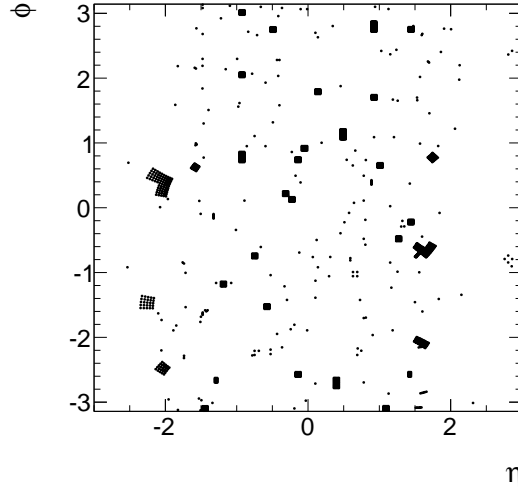


Figure 5.5: Visualisation of dead and noisy ECAL cells in the detector's $\phi - \eta$ plane according to [31, 32].

$p_T > 20 \text{ GeV}$ and $|\eta| < 2.3$ (see Section ?? for details on the tau reconstruction). Some loose isolation requirements are enforced to protect the tau reconstruction from jet contamination.

- ❖ The track must not be within a cone of $\Delta R < 0.5$ to a reconstructed jet ($p_T > 20 \text{ GeV}$ and $|\eta| < 4.5$).
- ❖ Veto tracks within a cone of $\Delta R < 0.05$ to a dead or noisy ECAL cell (visualised in

Table 5.3: Intermodule ECAL gaps.

η -ranges
$-1.14018 < \eta < -1.1439$
$-0.791884 < \eta < -0.796051$
$-0.44356 < \eta < -0.447911$
$0.00238527 < \eta < -0.00330793$
$0.446183 < \eta < 0.441949$
$0.793955 < \eta < 0.789963$
$1.14164 < \eta < 1.13812$

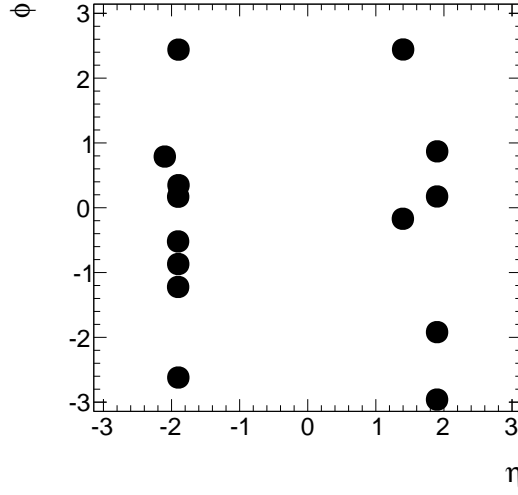


Figure 5.6: Visualisation of bad cathode strip chambers in the detector's $\phi - \eta$.

Fig. 5.5).

- ❖ Veto tracks that point towards the direction of the ECAL intermodule gap listed in Table 5.3.
- ❖ Veto tracks that point towards a bad CSC (visualised in Fig. 5.6).
- ❖ Veto tracks that point towards the region between ECAL barrel and endcap at $1.42 < |\eta| < 1.65$

These lepton and jet veto selection requirements are of course highly suppressing the background emerging from real lepton/jet production like in $W + \text{jets}$ events. The discrimination power of the lepton and jet vetos is shown in Fig. 5.7 where the minimum ΔR between the candidate track and a reconstructed electron, muon, tau or jet is shown.

Finally, two further characteristics of chargino tracks are exploited. As the chargino is produced in a very clean environment, the isolation of the track can discriminate signal against background events.

Furthermore, for charginos decaying inside the tracker there is no associated energy deposition in the calorimeters in the direction of the track. This is a very pronounced characteristics of signal tracks.

The resulting selection cuts are as follows

- ❖ No further substantial track activity (less than 10%) is allowed in a cone of $\Delta R < 0.3$ around the candidate track: $\sum_{\Delta R < 0.3} p_T / p_T^{\text{cand}} < 0.1$

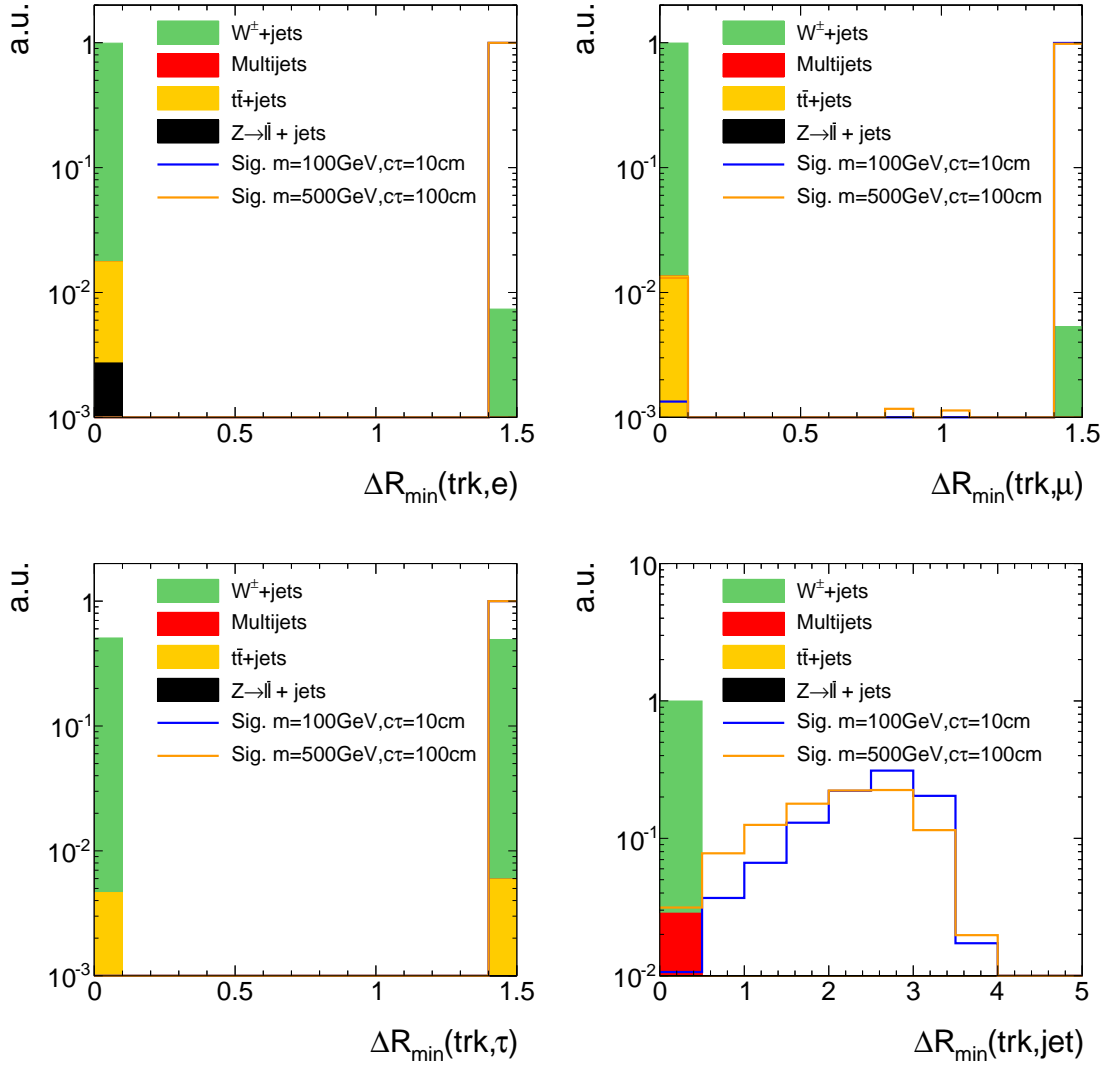


Figure 5.7: The minimum ΔR between the candidate track and a reconstructed electron (top left), muon (top right), tau (bottom left) or jet (bottom right) after the full candidate track selection cuts besides the one shown in the corresponding plot.

- ❖ Little calorimeter energy deposits (ECAL+HCAL) in a cone of $\Delta R < 0.5$ around the track: $E_{\text{calo}}^{\Delta R < 0.5} < 5 \text{ GeV}$.

The discrimination power of these two variables is shown in Fig. 5.8.

As emphasised before, this analysis aims at being sensitive especially on shorter lifetimes. Still, in order to allow for charginos decaying at any layer of the tracker, no explicit selection cut on the number of missing outer hits is required.

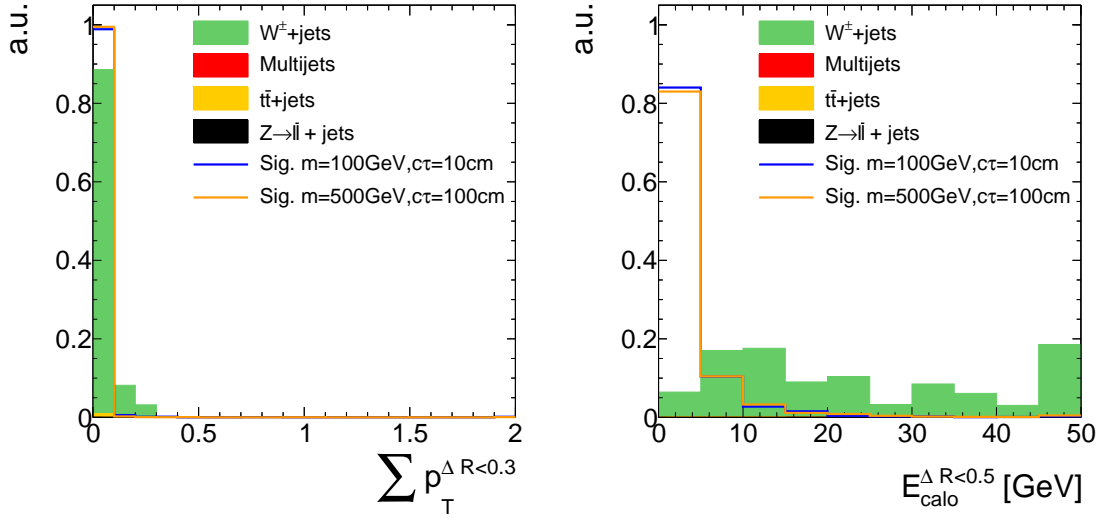


Figure 5.8: Track isolation (left) and calorimeter energy deposits (right) of the candidate track after the full previous selection.

An overview over the full analysis preselection is given in Table 5.4. A summary table of the event yields after each selection step for the simulated background datasets and for some of the signal models can be found in Appendix A.

Given the presented signal candidate selection, a set of two variables remain that are highly discriminating: The transverse momentum p_T and the energy release per path length dE/dx of the candidate track. In this analysis, the Asymmetric Smirnov discriminator I_{as} is used to enhance the discriminating power of dE/dx . See Section ?? for the definition and a detailed explanation of I_{as} . In Fig. 5.9, the distribution of the remaining two variables are shown after the application of the full signal candidate selection. These variables are used to optimise the sensitivity of the search. The optimisation process will be explained in Section 7. However, before the optimisation can be accomplished, a characterisation and estimation of the background is needed. This topic will be discussed in the following section.

Table 5.4: Summary and categorisation of the analysis selection.

Trigger	HLTMonoCentralPFJet80_PFMETnoMu95_NHEF0p95 HLTMonoCentralPFJet80_PFMETnoMu105_NHEF0p95 HLT_MET120_HBHENoiseCleaned	
Event-based selection	Trigger selection	$p_T^{1.\text{jet}} > 100 \text{ GeV}$ with $ \eta_{1.\text{jet}} < 2.4$, $\text{CHF}_{1.\text{jet}} > 0.2$, $\text{CEF}_{1.\text{jet}} < 0.5$, $\text{NHF}_{1.\text{jet}} < 0.7$, $\text{NEF}_{1.\text{jet}} < 0.7$ $\cancel{E}_T > 100 \text{ GeV}$
	QCD suppression	$\Delta\phi_{\max}(\text{jet}_i, \text{jet}_j) < 2.7$ for all jets with $p_T > 20 \text{ GeV}$, $ \eta < 4.5$ $\Delta\phi_{\max}(\text{jet}_i, \cancel{E}_T) > 0.5$ for two leading jets
Candidate track selection	≥ 1 track that fulfils the following criteria:	
	Good quality selection	high-purity as defined in [22] $N_{\text{miss}}^{\text{middle/inner}} = 0$ $ d0 < 0.02 \text{ cm}$ $ dz < 0.5 \text{ cm}$
	Kinematic selection	$ \eta < 2.1$ $p_T > 10 \text{ GeV}$
	Lepton/jet veto	No muon within $\Delta R < 0.15$ No electron within $\Delta R < 0.15$ No tau within $\Delta R < 0.15$ No jet within $\Delta R < 0.5$ No dead/noisy ECAL cell within $\Delta R < 0.05$ Not within an ECAL intermodule gap Not within $1.42 < \eta < 1.65$ Not within $\Delta R < 0.25$ to a bad CSC
	Isolation selection	$\sum_{\Delta R < 0.3} p_T / p_T^{\text{cand}} < 0.1$ $E_{\text{calo}}^{\Delta R < 0.5} < 5 \text{ GeV}$

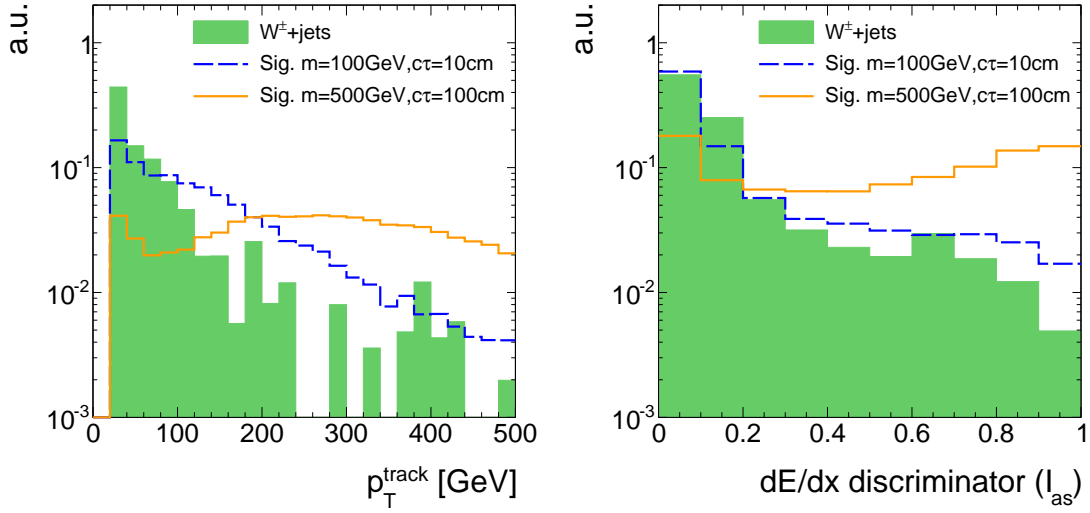


Figure 5.9: Candidate track p_T (left) and I_{as} (right) after the full signal candidate selection for signal and $W + \text{jets}$ events. Because of the low statistical precision of the $W + \text{jets}$ sample, the trigger requirements are not applied. This does not influence the shape of the distributions since \cancel{E}_T and $p_T^{1,\text{jet}}$ are not expected to be correlated with the track characteristics.

6 Characterisation and estimation of the Standard Model backgrounds

After the application of the signal candidate selection, explained in the previous section, the background arising from Standard Model processes is dramatically reduced. Only two events in the simulated $W + \text{jets}$ sample remain. One of these originates from an unreconstructed muon, the other one from an unreconstructed electron. This implies, that the electron, muon, and tau vetos cannot reject all leptons because some are not properly reconstructed. Due to the limited size of the simulated $W + \text{jets}$ dataset (15 times smaller than the number of events expected from $W + \text{jets}$ processes during 2012 data taking), it is not possible to rely on a full simulation-based estimation of the leptonic background. The underlying mechanism of the non-reconstruction of a lepton and the corresponding methods to estimate the leptonic background will be explained in detail in Section 6.2.

Furthermore, there is the possibility that a track is reconstructed out of a set of hits

that do not origin from only one single particle. Such tracks are called “fake tracks”. Background tracks arising from a combination of unrelated hits will be explained in the following Section 6.1. It should be noted that the fake background is contributing through all SM processes, not only via $W + \text{jets}$. Still, as the characteristics of fake tracks are independent of the underlying process, this background can also be studied on simulation using $W + \text{jets}$ events only.

6.1 Fake background

Fake tracks are tracks that are not reconstructed out of the trajectory of one single particle. The rate at which this wrong reconstruction occurs is highly restrained by the quality cuts on χ^2 and the vertex compatibility of the track reconstruction algorithm. Details on the reconstruction algorithm of tracks at CMS can be found in Section ??.

The probability of reconstructing a fake track is strongly correlated with the number of hits in the tracker system. This can be seen in Fig. 6.1, where the normalised distribution of the number of hits from fake tracks is depicted. There are almost no fakes with a number of hits larger than seven. In simulation, fake tracks are defined as tracks that cannot be matched to a generator-level particle within a distance of $\Delta R < 0.01$.

Fakes are efficiently suppressed by the requirements of no missing middle or inner hits and the compatibility with the primary vertex. Unfortunately, wrongly reconstructed tracks which pass these criteria, do also easily pass the $E_{\text{calo}}^{\Delta R < 0.5} < 5 \text{ GeV}$ requirement

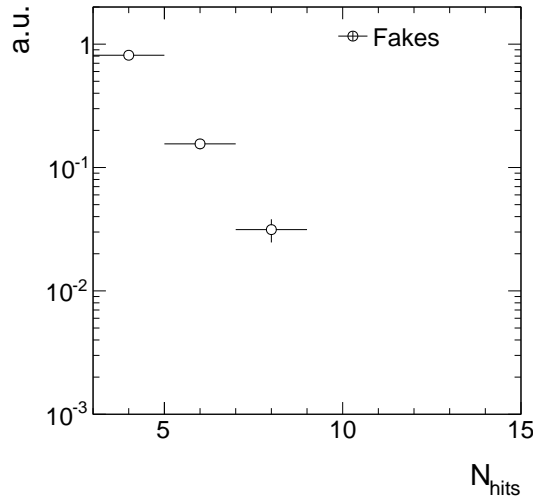


Figure 6.1: Normalised distribution of the number of hits for fake tracks after the signal candidate selection from Table 5.4. To increase the statistical precision, only track selection requirements are applied.

with high efficiency.

In this analysis, the estimation of the fake background is split into two parts. First, the background is determined inclusively in dE/dx . Second, the dE/dx (I_{as}) distribution is estimated with the help of a fake enriched control region. This second step is needed to enable an optimisation in dE/dx (see Section 7).

Inclusive fake background estimation

The inclusive background estimation closely follows the background estimation method done in [31,32]. It aims at determining the probability of having a fake track in an event that passes the full signal candidate selection (Table 5.4) plus a potential additional p_T selection cut that is determined in an optimisation procedure (Section 7). This probability will be called the fake rate ρ_{fake} .

The inclusive fake background is estimated with the help of $Z \rightarrow \mu\bar{\mu}$ and $Z \rightarrow e\bar{e}$ events from data. $Z \rightarrow \ell\bar{\ell}$ events can be selected with high purity by requiring two well reconstructed muons or electrons that are opposite in charge and for which the invariant mass is around the Z -boson mass of ~ 90 GeV. As these events do not contain further leptons from the hard interaction, any additional track is either an ISR jet, a soft particle from the underlying event or is a fake, reconstructed out of a combination of several soft particles. Since the track-based signal candidate selection requires a track with a $p_T > 20$ GeV that is no lepton or jet, it suppresses ISR jets and soft tracks from the underlying event. Thus, applying the track-based signal candidate selection on $Z \rightarrow \ell\bar{\ell}$ events selects fake tracks with high purity.

The selection of two well reconstructed muons and electrons is done with the single-muon and single-electron datasets listed in Table 6.1. For the $Z \rightarrow \mu\bar{\mu}$ selection an event is required to have two muons with $p_T > 25$ GeV and $|\eta| < 2.4$. To suppress background from cosmic muons, the distance from the primary vertex must be less than $|d0| < 0.2$ cm in radial and $|dz| < 0.5$ cm in longitudinal direction. In order to suppress background arising from jets that fake muons, various quality criteria are applied: it is required that there is at least one hit in the muon detector that is considered in the global muon fit, and that at least two measurements are from different muon detector stations. Concerning the track of the muon in the tracker system, at minimum one hit in the pixel tracker and at least six hits in the full tracker system are required. An isolation criterion is applied that requires the sum of transverse momenta of all particle-flow particles in a cone of $\Delta R < 0.4$ around the muon to be less than 12%. Finally, the muons are required to be opposite in charge and to have an invariant mass between 80 – 100 GeV. The $Z \rightarrow \mu\bar{\mu} + \text{fake track}$ selection is summarised in Table 6.2.

In order to select $Z \rightarrow e\bar{e}$ events in data, the two electrons are required to have

Table 6.1: Datasets used for the determination of the fake rate.

Dataset	Luminosity [fb^{-1}]
/SingleMu/Run2012A-22Jan2013-v1/AOD	0.876
/SingleMu/Run2012B-22Jan2013-v1/AOD	4.405
/SingleMu/Run2012C-22Jan2013-v1/AOD	7.040
/SingleMu/Run2012D-22Jan2013-v1/AOD	7.369
/SingleElectron/Run2012A-22Jan2013-v1/AOD	0.876
/SingleElectron/Run2012B-22Jan2013-v1/AOD	4.412
/SingleElectron/Run2012C-22Jan2013-v1/AOD	7.050
/SingleElectron/Run2012D-22Jan2013-v1/AOD	7.368

$p_T > 25 \text{ GeV}$, $|\eta| < 2.5$ and no missing hits in the inner layers of the tracker. Furthermore, the electrons need to pass a conversion veto as described in [36] in order to reduce background arising from photon conversions. An isolation requirement similar to the muon isolation criterion is applied with an increased threshold of 15%. The electron identification is further based on a multivariate technique developed within [37] that exploits electron characteristics about the track quality, the ECAL cluster shapes, and the combination of the measurements in the tracker and in the ECAL. Again, the two electrons must be opposite in charge and their invariant mass must be between $80 - 100 \text{ GeV}$. A summary of the $Z \rightarrow e\bar{e} + \text{fake track}$ event selection can be found in Table 6.3.

When applying a $Z \rightarrow \ell\bar{\ell}$ selection plus the candidate track selection, the selected track should be a fake. If this is indeed the case can be tested on simulated $Z \rightarrow \ell\bar{\ell}$ events. As can be seen in Fig. 6.2, a reasonable purity in fake tracks can be achieved by applying the candidate track selection on top of the $Z \rightarrow \ell\bar{\ell}$ selection. In simulated $Z \rightarrow \mu\bar{\mu}$ events, a purity of 88%, whereas in simulated $Z \rightarrow e\bar{e}$ events a purity of 92% of fake tracks can be achieved.

As already mentioned, the fake rate is defined as the probability that an event contains a fake track that fulfils the candidate track selection. Thus, for the $Z \rightarrow \ell\bar{\ell}$ datasets it is defined as the number of events passing the full selection described in Table 6.2 (Table 6.3) divided by the number of events that pass only the event-based selection in

Table 6.2: Event selection cuts for the $Z \rightarrow \mu\bar{\mu} + \text{fake}$ control sample to estimate the inclusive fake background.

Event-based selection	<p>Two global muons with $p_T > 25 \text{ GeV}$</p> <p>$\eta < 2.4$</p> <p>$\sum_{\Delta R < 0.4} p_T^{\text{PF particle}} / p_T(\mu) < 0.12$</p> <p>$\left. \frac{\chi^2}{ndof} \right _{\text{global track}} < 10$</p> <p>$d0 < 0.2 \text{ cm}$</p> <p>$dz < 0.5 \text{ cm}$</p> <p>$\geq 1$ hit in the muon detector considered in global fit</p> <p>≥ 2 hits in different muon stations</p> <p>≥ 1 hit in the pixel detector</p> <p>≥ 6 hits in the tracker system</p> <p>Muons opposite in charge</p> <p>$80 \text{ GeV} < M_{\text{inv}}(\mu_1, \mu_2) < 100 \text{ GeV}$</p>
Candidate track selection	<p>Good quality selection</p> <p>Kinematic selection</p> <p>Lepton/jet veto</p> <p>Isolation selection</p>

Table 6.2 (Table 6.3)

$$\rho_{\text{fake}} = \frac{N_{Z \rightarrow ll}^{\text{cand trk selection}}}{N_{Z \rightarrow ll}}$$

Fake rates are determined independently for the $Z \rightarrow \mu\bar{\mu} + \text{fake}$ and $Z \rightarrow e\bar{e} + \text{fake}$ event selection and then averaged to obtain the final fake rate. The fake rate with the candidate track selection given in Table 5.4 is $(6.86 \pm 0.25) \cdot 10^{-5}$. This is not the final result as the optimisation in p_T will add an additional p_T selection cut to the candidate track selection.

Within [31,32], it was checked that the fake rate is constant for different processes. This is shown in Fig. 6.3 where the fake rate is depicted for the most important SM processes. Since the fake rate is constant for different SM processes, the fake rate determined on the $Z \rightarrow \ell\bar{\ell}$ dataset can be generalised for all SM background possibly contributing to this

Table 6.3: Event selection cuts for the $Z \rightarrow e\bar{e} + \text{fake}$ control sample to estimate the inclusive fake background.

Event-based selection	Two Electrons with $p_T > 25 \text{ GeV}$ $ \eta < 2.5$ $\sum_{\Delta R < 0.4} p_T^{\text{PF particle}} / p_T(e) < 0.15$ pass conversion veto [36] no missing inner tracker hits good MVA electron as defined in [37] Electrons opposite in charge $80 \text{ GeV} < M_{\text{inv}}(e_1, e_2) < 100 \text{ GeV}$
Candidate track selection	Good quality selection Kinematic selection Lepton/jet veto Isolation selection

search. Thus, the inclusive fake background can be estimated by multiplying the fake rate with the number of events selected from the MET dataset (Table 5.2) by applying the event-based signal candidate requirements from Table 5.4.

$$N_{\text{bkg}}^{\text{fake, inclusive in } I_{\text{as}}} = \rho_{\text{fake}} \cdot N_{\text{event-based selection}}^{\text{MET}}$$

Given the number of events after the event-based selection of $N_{\text{event-based selection}}^{\text{MET}} = 1.38 \cdot 10^6$ and the fake rate cited above, the inclusive fake background can be estimated to 94.7 ± 3.4 for the candidate track selection.

It should be noted again that the inclusive fake background estimation will be only inclusive in I_{as} not in p_T . That means that after the definition of the signal region, $N_{\text{bkg}}^{\text{fake, inclusive in } I_{\text{as}}}$ is determined with the additional optimal p_T selection.

Possible differences between the fake rate in $Z \rightarrow \ell\bar{\ell}$ events and other SM processes are estimated on simulated events and taken into account as a systematic uncertainty (see Section 6.4.1).

dE/dx shape of fake background

The information about the energy release per path length for fake tracks should not be taken from simulated samples as the simulation of dE/dx is not reliable (cf. Fig. 3.9). Within this analysis the Asymmetric Smirnov discriminator I_{as} is used to discriminate signal against background with respect to dE/dx (see Section 3.3). In order to estimate the I_{as} shape of fake tracks, a control region $\text{CR}_{I_{\text{as}}}^{\text{fake}}$ is defined that is enriched with fakes and shows the same I_{as} distribution as fake tracks in the signal region.

To enrich fake tracks, it is possible to invert the selection cuts on the number of missing middle and inner hits, i.e. requiring at least one missing inner or middle hit ($N_{\text{miss}}^{\text{inner}} + N_{\text{miss}}^{\text{middle}} > 0$). Figure 6.4 shows the distribution of the number of missing inner plus missing middle hits for fake and leptonic tracks in simulated $W + \text{jets}$ events. It can be seen that the enrichment of fakes by this selection works. The resulting purity of fakes in $\text{CR}_{I_{\text{as}}}^{\text{fake}}$ is about 98% (see Fig. 6.5).

Additionally, it must be checked whether the I_{as} shape in $\text{CR}_{I_{\text{as}}}^{\text{fake}}$ is comparable to the I_{as} shape in the signal region. As the exact definition of the signal region will be addressed during optimisation, this test is done for various p_{T} selection cuts.

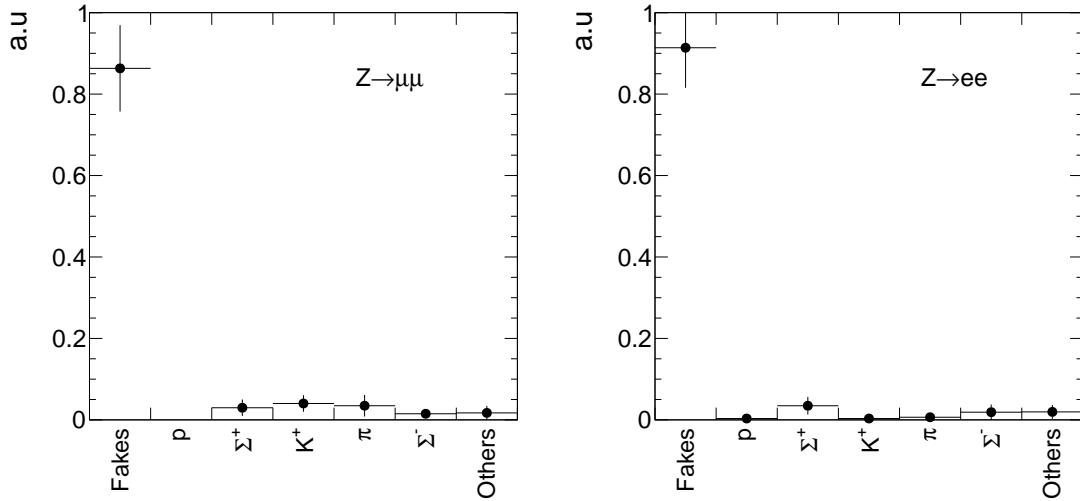


Figure 6.2: Corresponding generator-level particles of all tracks within $Z \rightarrow \ell\bar{\ell} + \text{fake}$ that were selected according to the candidate track selection. The full selection for tracks in $Z \rightarrow \mu\bar{\mu}$ events (left) is given in Table 6.2. The full selection for tracks in $Z \rightarrow e\bar{e}$ events (right) is given in Table 6.3. “Fake” means that no corresponding generator-level particle is found.

The comparison of the I_{as} shape of fake tracks can only be done on simulation. Thus, simulated $W + \text{jets}$ events are used to select fake tracks in both regions. A comparison of the shape for the candidate track selection and the $\text{CR}_{I_{\text{as}}}^{\text{fake}}$ is shown in Fig. 6.5.

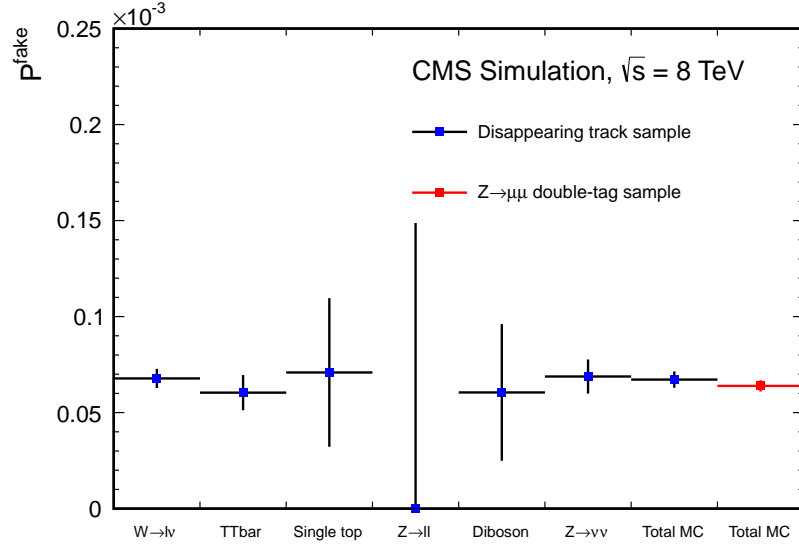


Figure 6.3: Fake track rate estimated in [31,32] for tracks with four hits. Taken from [32]

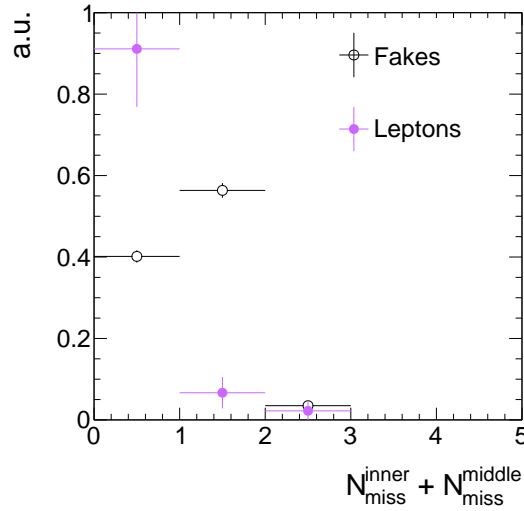


Figure 6.4: Normalised number of missing inner plus missing middle hits for fake and leptonic tracks for the full candidate track selection with the selection requirements on $N_{\text{miss}}^{\text{inner}}$ and $N_{\text{miss}}^{\text{middle}}$ removed. Trigger requirements and QCD suppression cuts were removed to enhance the statistical precision.

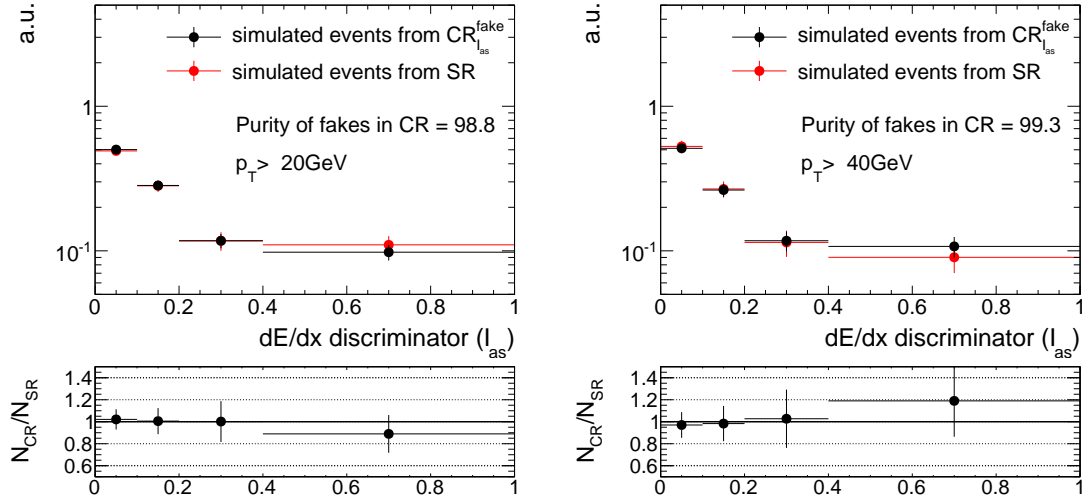


Figure 6.5: Comparison of the I_{as} shape between $\text{CR}_{I_{\text{as}}}^{\text{fake}}$ and the signal region for two different track p_{T} selections of $p_{\text{T}} > 20 \text{ GeV}$ (left) and $p_{\text{T}} > 40 \text{ GeV}$ (right). To enhance the statistical precision only the track-based selection is applied.

The I_{as} shape is almost identical in the signal and in the control region which makes the definition of the control region perfectly for estimating the I_{as} shape from $\text{CR}_{I_{\text{as}}}^{\text{fake}}$ in data. The remaining shape differences are taken into account as a systematic uncertainty (discussed in Section 6.4.2).

6.2 Leptonic background

The leptonic background of the here presented search is caused by non-reconstructed leptons that circumvent the lepton veto selection. However, at least non-reconstructed electrons or taus should in principle deposit enough energy in the calorimeters such that they can still be vetoed by the calorimeter isolation requirement $E_{\text{calo}}^{\Delta R < 0.5} < 5 \text{ GeV}$. As muons don't deposit much energy in the calorimeters, this reasoning does not apply to them. In the following, the sources of the three different leptonic backgrounds are characterised.

Electrons

To reject unreconstructed electrons, all tracks pointing to a dead or noisy ECAL cell, to an ECAL intermodule gap, or to the region between ECAL barrel and endcap at $1.42 < |\eta| < 1.65$ are vetoed, as described in Section 5.2. By this selection, almost all electrons are efficiently rejected. In the simulated W +jets sample only one simulated event remains that passes all signal candidate selection criteria and for which the candidate track can be matched to a generator-level electron. This event is visualised in Fig. 6.6.

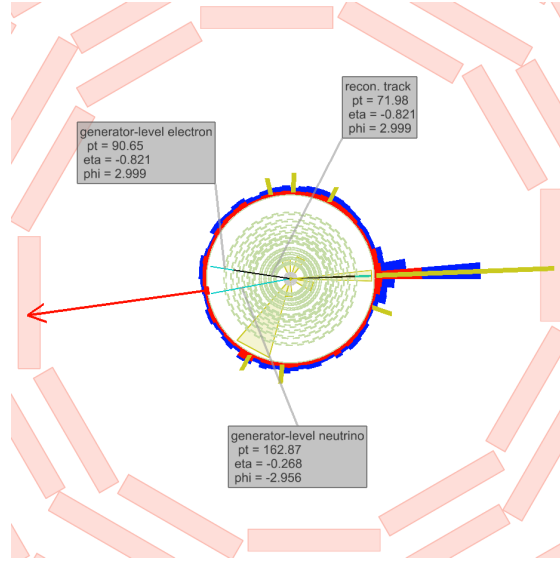


Figure 6.6: Visualisation of a $W \rightarrow e\nu_e$ event contributing to the SM background. In light blue, generator-level particles including e and ν_e of the W -boson decay are shown. The neutrino, only weakly interacting does not show any signature in the detector, whereas the electron ($p_T \simeq 90$ GeV) leaves a track (black line) with $p_T \simeq 70$ GeV in the tracker. No ECAL energy deposits in the direction of the electron are visible. This is caused by the fact that the corresponding ECAL energy deposits were not read out in this event. An ISR jet ($p_T \simeq 230$ GeV) causes the \cancel{E}_T (read arrow) in the event.

In this event no energy deposits in the ECAL are read out, which suggests that the corresponding ECAL tower was not working properly in 2012. Additionally, electrons can do bremsstrahlung which can change the direction of the electron significantly. Thus, the energy deposits in the ECAL can possibly not be matched to the original electron.

Taus

Taus are contributing to the leptonic background through the hadronic decay of a tau lepton to one charged pion $\tau \rightarrow \pi^\pm \nu_\tau$. Other decay modes of the tau lepton are suppressed by the track isolation criterion. Taus fail reconstruction if they don't deposit energy in the HCAL or ECAL. Unreconstructed taus can therefore also easily bypass the calorimeter isolation criterion. Because of nuclear interactions in the tracker, pions often result in short reconstructed tracks that can easily be highly mismeasured in p_T . Thus, taus can contribute to the background even if imposing a tight selection in the transverse momentum. Such an event is shown in Fig. 6.7.

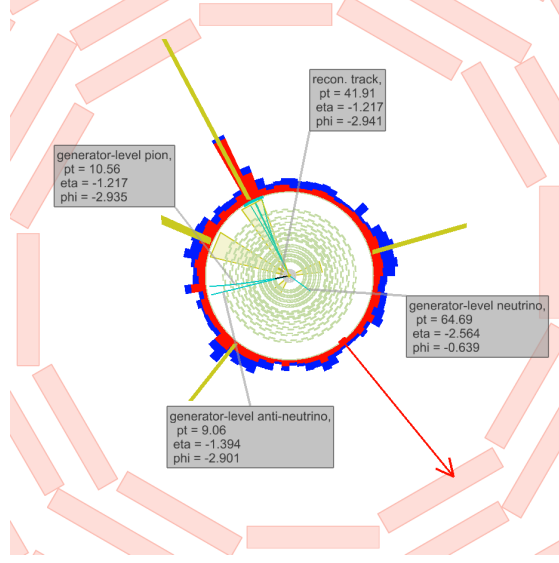


Figure 6.7: Visualisation of a $W^+ \rightarrow \tau^+ \nu_\tau \rightarrow \pi^+ \bar{\nu}_\tau \nu_\tau$ event contributing to the SM background. In light blue, the generator-level particles including π^+ , $\bar{\nu}_\tau$ and ν_τ are shown. The transverse momentum of the generator-level pion is only $p_T \sim 10$ GeV, but because the reconstructed track (black line) is very short, it leads to a high mismeasurement of the track p_T of ~ 40 GeV. The shortness of the track is caused by nuclear interactions of the pion. As no corresponding ECAL or HCAL energy deposits are measured, the reconstruction of the pion fails. The ISR jet causes the \cancel{E}_T (read arrow) in the event.

Muons

Muons can fail reconstruction if they point towards a bad cathode strip chamber. This is taken into account in the candidate track selection. However, some of the muons still fail reconstruction if they fall within the gap between stations 0 and 1 of the drift tube system at $|\eta| = 0.25$. The muon reconstruction efficiency drops from around 99% to a value of around 94% as shown in [31,32]. This possibility is illustrated in a simulated event shown in Fig. 6.8.

In [31,32] events are rejected if the track is pointing in a region of $0.15 < |\eta| < 0.35$. In this search, this cut was omitted to maximise signal acceptance. Due to the additional selection in I_{as} , muons can be efficiently suppressed. E.g. in the event shown in Fig. 6.8, the muon has an I_{as} value of about 0.007.

In general, all leptons are minimally ionising. However, as electrons are much lighter compared to muons or pions, they loose more energy also via radiative effects. Still, all three lepton types loose much less energy compared to hypothetical new heavy particles. To have the possibility to make an optimisation in the two main discriminating variables

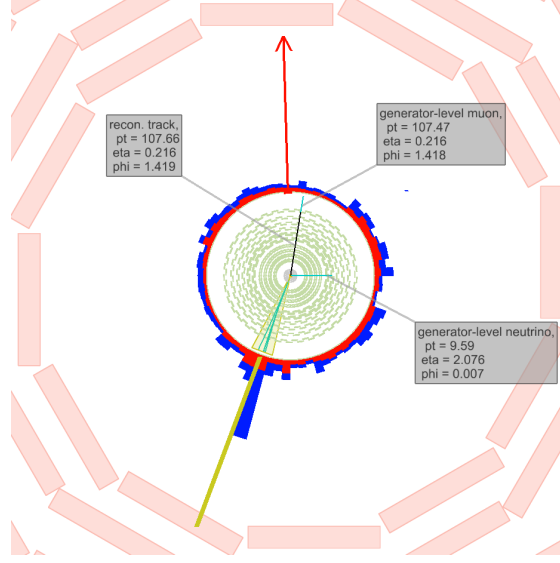


Figure 6.8: FIXME (show full picture)! Visualisation of an $W \rightarrow \mu\nu_\mu$ event contributing to the SM background. In light blue, the generator-level particles including μ and ν_μ of the W decay are shown. The muon is pointing to the η -region between stations 0 and 1 of the DT system at $|\eta| \sim 0.25$. In this region the muon reconstruction is less efficient. No signal in the muon chambers is visible. Therefore the muon could not be reconstructed. The ISR jet causes the \cancel{E}_T (read arrow) in the event.

p_T and I_{as} , the background estimation methods are designed to work for all different p_T and I_{as} selection cuts.

As for the fakes, the leptonic background estimation is splitted into two parts. First, the estimation of the inclusive background without I_{as} information. Second, the estimation of the I_{as} shape for all three leptonic background sources.

6.2.1 Inclusive leptonic background estimation

The inclusive (without I_{as} information) lepton background estimation method is similar to the background estimation method used in [31, 32].

In order to estimate the number of events in the signal region originating from unreconstructed leptons, information from simulated events is used. With the help of simulated $W + \text{jets}$ events, the ratio $\rho_{MC}^{\text{lep}_i}$ between the number of events in the signal region with the selected track matched to a generator-level lepton $N_{SR}^{\text{trk matched to lepton}_i}$ and the number of events in a control region $N_{CR}^{\text{lepton}_i \text{ veto inverted}}$ with a inverted lepton veto is determined.

For muons, this lead to the following expression

$$\rho_{\text{MC}}^{\mu} = \frac{N_{\text{SR,MC}}^{\text{trk matched to } \mu}}{N_{\text{CR,MC}}^{\mu \text{ veto inverted}}}.$$

Since for electrons and taus the reconstruction efficiency is highly correlated with the $E_{\text{calo}}^{\Delta R < 0.5}$ selection requirement, the $E_{\text{calo}}^{\Delta R < 0.5}$ requirement is additionally removed in the control regions for these two lepton types

$$\rho_{\text{MC}}^{e,\tau} = \frac{N_{\text{SR,MC}}^{\text{trk matched to } e,\tau}}{N_{\text{CR,MC}}^{e,\tau \text{ veto inverted, } \cancel{E_{\text{calo}}^{\Delta R < 0.5}} < 5 \text{ GeV}}}.$$

In order to estimate the inclusive background for all three lepton types, the scaling factor $\rho_{\text{MC}}^{\text{lep}_i}$ is applied to the number of events in the lepton veto inverted control region measured in data. Also in data the control region for electrons and taus is defined with the $E_{\text{calo}}^{\Delta R < 0.5}$ requirement removed. Thus, the inclusive number of predicted background events can be estimated with

$$N_{\text{bkg}}^{\mu, \text{ inclusive in } I_{\text{as}}} = \rho_{\text{MC}}^{\mu} \cdot N_{\text{CR,data}}^{\mu \text{ veto inverted}}.$$

for muons, and

$$N_{\text{bkg}}^{e,\tau, \text{ inclusive in } I_{\text{as}}} = \rho_{\text{MC}}^{e,\tau} \cdot N_{\text{CR,data}}^{e,\tau \text{ veto inverted, } \cancel{E_{\text{calo}}^{\Delta R < 0.5}} < 5 \text{ GeV}}.$$

for electrons and taus.

This method relies on the simulation of the lepton reconstruction efficiencies which is expected to be reasonably accurate [38–40]. For electrons and taus the simulation of the calorimeter isolation is utilised as well. Possible discrepancies between simulation and data are taken into account as a systematic uncertainty via a comparison of the lepton reconstruction efficiencies in data and simulation in $Z \rightarrow \ell\bar{\ell}$ events (see Section 6.4.3).

To reduce the statistical uncertainty, the scale factor is calculated without applying the QCD suppression cuts. After the signal candidate selection described in Section 5.2, only one event remains in the simulated $W + \text{jets}$ sample where the candidate track can be matched to an electron. There are five track candidates that can be matched to a muon, and zero selected tracks that can be matched to a pion. The statistical uncertainties are calculated as the 68% upper and lower limits on the inclusive background with the Neyman procedure [15, 41]. Table 6.4 gives the result for the prediction of the inclusive leptonic background for the signal candidate selection from Section 5.2.

Table 6.4: Scaling factor $\rho_{\text{MC}}^{\text{lep}_i}$, number of events in the data control region $N_{\text{CR,data}}$ and the resulting inclusive estimation $N_{\text{predicted}}$ after the candidate track selection.

	scaling factor $\rho_{\text{MC}}^{\text{lep}_i}$	$N_{\text{CR,data}}$	$N_{\text{predicted}}$
electrons	$1.25^{+1.70}_{-0.77} \cdot 10^{-4}$	60067	$7.49^{+10.19}_{-4.63}$
muons	$2.17^{+1.65}_{-0.93} \cdot 10^{-4}$	76664	$16.64^{+12.64}_{-7.12}$
taus	$< 2.13 \cdot 10^{-2}$	445	< 9.46

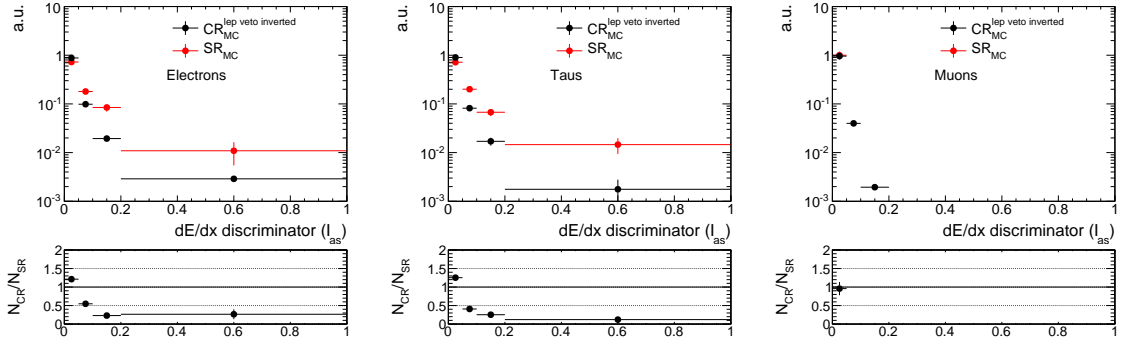


Figure 6.9: Normalised I_{as} distribution for electrons (left), pions from the tau decay (middle) and muons (right) in the signal region (red) and the lepton veto inverted control region (black).

6.2.2 dE/dx shape of leptonic background

In order to get information about the I_{as} (see Section 3.3) shape in the signal region of electrons, muons and taus, a control region must be found where the shape of the observable is at least similar to that in the signal region. The most natural control region, being the lepton veto inverted control region, cannot be used because the variable I_{as} is highly correlated to the lepton reconstruction efficiency, as can be seen in Fig. 6.9. The discrepancies reach factors up to an order of magnitude.

Various other control regions were tested and could not be used because of too large I_{as} shape differences to the signal region.

As no suitable control region exists where the I_{as} shape of the leptons is at least similar to the shape in the signal region, it is decided to use the I_{as} information from simulation. This introduces a large systematic uncertainty since dE/dx (and therefore I_{as}) is not simulated well. However, the corresponding systematic uncertainty is still smaller than

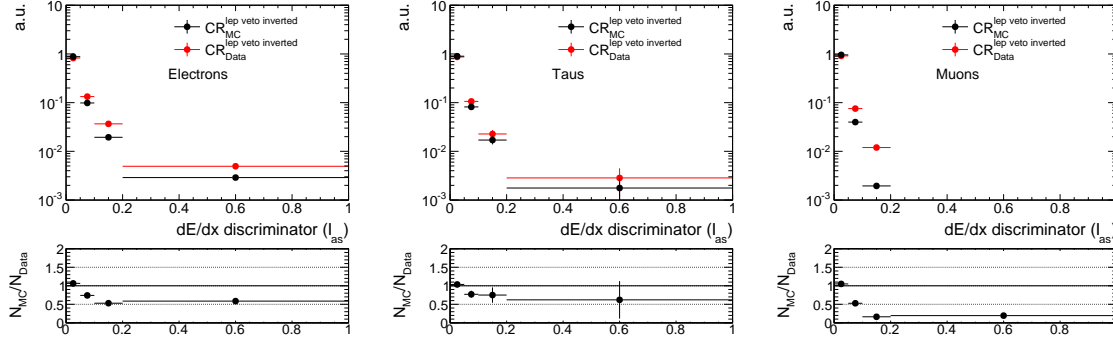


Figure 6.10: Normalised I_{as} distribution for electrons (left), pions from the tau decay (middle) and muons (right) in the lepton veto inverted control region from simulated (black) and real (red) events.

taking the I_{as} shape from a control region in data: compare Fig. 6.9 and Fig. 6.10.

In order to take into account the bias when using I_{as} from simulation, a systematic uncertainty is estimated that addresses simulation-data differences of the I_{as} distributions. This systematic uncertainty is discussed in Section 6.4.4.

6.3 Background estimation validation

The background estimation methods are exhaustively validated with the help of signal depleted control regions. Various control regions are used for validation.

First, to validate the estimation method of the leptonic background, a leptonic control region is defined by selecting only tracks with a minimum number of seven hits in the tracker. This reduces the fake contribution to a minimum (cf. Fig. 6.1). Additionally in order to minimise signal contamination, the calorimeter isolation requirement is inverted to $E_{calo}^{\Delta R < 0.5} > 10 \text{ GeV}$. The validation test for the control region with $E_{calo}^{\Delta R < 0.5} > 10 \text{ GeV}$ and $N_{hits} > 6$ is shown in Table C.3. The predicted number of events by the leptonic background estimation is compatible with the observed data yield.

As the fake background can only be estimated within the low calorimeter isolation region ($E_{calo}^{\Delta R < 0.5} < 10 \text{ GeV}$) to ensure high fake purity, the information about the number of fake tracks in the high calorimeter isolation region is taken from the fake enriched control region $CR_{I_{as}}^{fake}$ defined in Section 6.1. In this control region, the ratio of $N_{E_{calo}^{\Delta R < 0.5} > 10 \text{ GeV}} / N_{E_{calo}^{\Delta R < 0.5} < 10 \text{ GeV}}$ is estimated and taken as a multiplicand to the number of events predicted from the $E_{calo}^{\Delta R < 0.5} < 10 \text{ GeV}$ region. In Table 6.6, two different validation tests are shown, once an inclusive validation in I_{as} and once with an I_{as} selection of 0.2. Again, the predicted background events is in agreement with the number of observed

Table 6.5: Validation test of leptonic background estimation. Left: $E_{\text{calo}}^{\Delta R < 0.5} > 10 \text{ GeV}$ and $N_{\text{hits}} > 6$. Right: $E_{\text{calo}}^{\Delta R < 0.5} > 10 \text{ GeV}$, $N_{\text{hits}} > 6$ and $I_{\text{as}} > 0.2$. Only statistical uncertainties are included.

	Predicted Yield	Data Yield		Predicted Yield	Data Yield
Total bkg	$132.68^{+26.31}_{-18.43}$	156	Total bkg	$0.0^{+0.50}_{-0.0}$	1
Electrons	$14.67^{+11.16}_{-6.29}$		Electrons	$0.0^{+0.07}_{-0.0}$	
Muons	$7.99^{+10.90}_{-5.00}$		Muons	$0.0^{+0.32}_{-0.0}$	
Taus	$109.04^{+21.18}_{-16.58}$		Taus	$0.0^{+0.38}_{-0.0}$	

events.

The whole validation is done for different selections in p_T and I_{as} . All validation tests show good agreement and can be found in Appendix C.

Still, systematic uncertainties need to be estimated. The sources of systematic uncertainties and how they are estimated will be explained in the following section.

Table 6.6: Validation test of fake and leptonic background estimation methods. Left: $E_{\text{calo}}^{\Delta R < 0.5} > 10 \text{ GeV}$. Right: $E_{\text{calo}}^{\Delta R < 0.5} > 10 \text{ GeV}$ and $I_{\text{as}} > 0.2$. Only statistical uncertainties are included.

	Predicted Yield	Data Yield		Predicted Yield	Data Yield
Total bkg	$309.00^{+33.46}_{-26.62}$	324	Total bkg	$14.80^{+2.92}_{-2.85}$	16
Electrons	$59.92^{+16.11}_{-11.85}$		Electrons	$0.75^{+0.36}_{-0.25}$	
Muons	$8.04^{+10.97}_{-5.03}$		Muons	$0.00^{+0.32}_{-0.00}$	
Taus	$173.06^{+24.62}_{-20.23}$		Taus	$2.33^{+0.74}_{-0.55}$	
Fakes	$67.98^{+11.57}_{-11.57}$		Fakes	$11.72^{+2.79}_{-2.79}$	

6.4 Systematic uncertainties

Systematic uncertainties on the background estimation include:

- the uncertainty on the fake rate ρ_{fake} ;
- the uncertainty on the I_{as} shape of fake tracks predicted from a control region;
- the uncertainty on the leptonic scale factor $\rho_{\text{MC}}^{\text{lep}_i}$ determined with simulated events;
- the uncertainty on the I_{as} shape of the leptonic background.

6.4.1 Uncertainty on the fake rate

The fake rate ρ_{fake} is determined with the help of observed $Z \rightarrow \ell\bar{\ell}$ events. To estimate the uncertainty on this fake rate caused by differences in the fake rate between different underlying processes, a comparison between the fake rate in simulated $Z \rightarrow \ell\bar{\ell} + \text{jets}$ and simulated $W + \text{jets}$ events is done. The fake rate in the $Z \rightarrow \ell\bar{\ell} + \text{fake track control}$ samples (see Tables 6.2 and 6.3) and the fake rate in the signal candidate selection from Table 5.4 in $W + \text{jets}$ events are compared.

Unfortunately, the statistical precision of the simulated $W + \text{jets}$ dataset is limited. Thus, the estimation of the systematic uncertainty is mainly driven by statistical uncertainties. In order to enhance the statistical precision of the estimation, the selection requirements on \cancel{E}_{T} and $p_{\text{T}}^{1.\text{jet}}$ are loosened and the QCD suppression requirements are removed. As these variables are not expected to be correlated with the fake rate, the relative uncertainty of the fake rate should stay the same. That this is indeed the case, can be seen in Table 6.7.

Table 6.7: Fake rates in simulated $W + \text{jets}$ and $Z \rightarrow \ell\bar{\ell} + \text{jets}$ events for different event-based selections of the $W + \text{jets}$ sample. The track-based selection is the candidate track selection from Table 5.4.

$W + \text{jets}$ selection	$\rho_{\text{fake}}^{W+\text{jets}}$	$\rho_{\text{fake}}^{Z \rightarrow \ell\bar{\ell}}$
$\cancel{E}_{\text{T}} > 100 \text{ GeV}, p_{\text{T}}^{1.\text{jet}} > 110 \text{ GeV}$	$(3.16^{+4.26}_{-1.94}) \cdot 10^{-5}$	$(3.17 \pm 0.21) \cdot 10^{-5}$
$\cancel{E}_{\text{T}} > 0 \text{ GeV}, p_{\text{T}}^{1.\text{jet}} > 70 \text{ GeV}$	$(3.03 \pm 0.68) \cdot 10^{-5}$	$(3.17 \pm 0.21) \cdot 10^{-5}$
$\cancel{E}_{\text{T}} > 0 \text{ GeV}, p_{\text{T}}^{1.\text{jet}} > 70 \text{ GeV}, \text{ no QCD cuts}$	$(3.05 \pm 0.44) \cdot 10^{-5}$	$(3.17 \pm 0.21) \cdot 10^{-5}$

The systematic uncertainty is estimated as the 1-sigma deviation of the ratio $\rho_{\text{fake}}^{W+\text{jets}} / \rho_{\text{fake}}^{Z \rightarrow \ell\bar{\ell}}$ from 1. For the candidate track selection, this is estimated to $\rho_{\text{fake}}^{W+\text{jets}} / \rho_{\text{fake}}^{Z \rightarrow \ell\bar{\ell}} = 0.96 \pm 0.16$ leading to a systematic uncertainty of 20%.

6.4.2 Uncertainty on the dE/dx shape of fake tracks

The systematic uncertainty on the shape of the I_{as} distribution takes into account the differences between the I_{as} shape in the fake control region $CR_{I_{as}}^{fake}$ and in the signal region. For the estimation, information from simulated $W + \text{jets}$ events is used. A comparison between the simulated I_{as} shape in the signal and in the control region can be seen in Fig. 6.11. To enhance the statistical precision only track-based selection cuts are applied.

The 1-sigma difference of the ratio of the number of events in the signal region and the control region from one is taken as systematic uncertainty. For a signal region definition with $p_T > 20 \text{ GeV}$ and $I_{as} > 0.2$ this corresponds to an uncertainty of around 21% and for a definition with $p_T > 40 \text{ GeV}$ and $I_{as} > 0.2$ of around 25%.

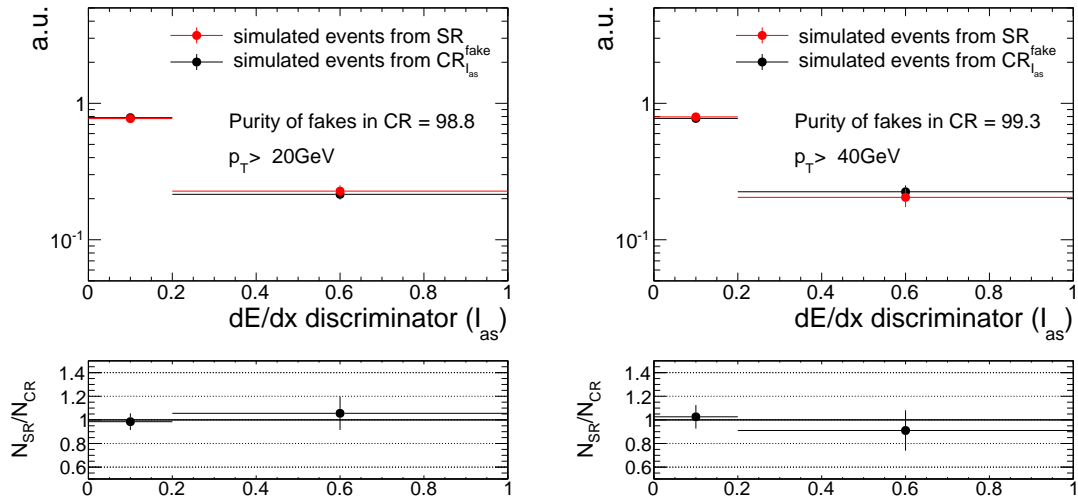


Figure 6.11: Underlying histograms to estimate the fake I_{as} systematic uncertainty. Normalised distributions of the I_{as} shape of fake tracks in the signal and control region of simulated $W + \text{jets}$ events with a p_T selection of 20 GeV (left) and a 40 GeV (right).

6.4.3 Uncertainty on the leptonic scale factor

The leptonic scale factor $\rho_{MC}^{lep_i}$ is estimated on simulated $W + \text{jets}$ events. The corresponding systematic uncertainty that addresses the use of information from simulation is derived by a “tag-and-probe” method conducted on real data and simulated events.

For this method a selection of $Z \rightarrow \ell\bar{\ell}$ events is done with one “tagged” well reconstructed lepton and one “probed” candidate track. To ensure a selection of $Z \rightarrow \ell\bar{\ell}$ events, a selection on the invariant mass of the reconstructed lepton and the candidate track is applied with $80 \text{ GeV} < M_{inv}(\text{lepton, cand. trk}) < 100 \text{ GeV}$ for muons and electrons. For taus, a muon from a $\tau \rightarrow \mu\nu\nu$ decay is selected with $40 \text{ GeV} < M_{inv}(\mu, \text{cand. trk}) < 75 \text{ GeV}$ and

$m_T(\mu, \cancel{E}_T) < 40 \text{ GeV}$ [31,32]. Furthermore, the candidate track and the lepton are required to be opposite in charge. As for the determination of the tau and electron scale factor with simulated $W + \text{jets}$ events, no requirement on the calorimeter isolation is applied. In order to reduce the contamination of fakes in the “tag-and-probe” samples an additional selection on the number of hits of $N_{\text{hits}} > 5$ is required. The selection requirements for the three tag-and-probe samples are listed in Tables B.1, B.2 and B.3 in Appendix B.

FIXME !The leptonic scale factors For the calculation of the leptonic scale factors, The selection is applied on simulated $Z \rightarrow \ell\bar{\ell}$ events and on real data from the single-muon and single-electron samples listed in Table 6.1. The largest difference of the ratio $\rho_{\text{MC}}^{\text{lep}_i} / \rho_{\text{Data}}^{\text{lep}_i}$ from unity is taken as systematic uncertainty. This results for the signal candidate selection in an uncertainty of 69% for the electron, 39% for the muon and 79 % for the tau scale factor.

6.4.4 Uncertainty on the leptonic dE/dx shape

The uncertainty on lepton I_{as} shape is estimated by a comparison of the I_{as} shape in data and simulation in the lepton veto inverted control region. Figure 6.12 shows the leptonic I_{as} distributions for all three lepton types in the lepton veto inverted control region in data and simulation. The 1-sigma difference of the ratio of the number of events in the control region in data and simulation from 1 is taken as systematic uncertainty. This leads to uncertainties between FIXME for the signal candidate selection.

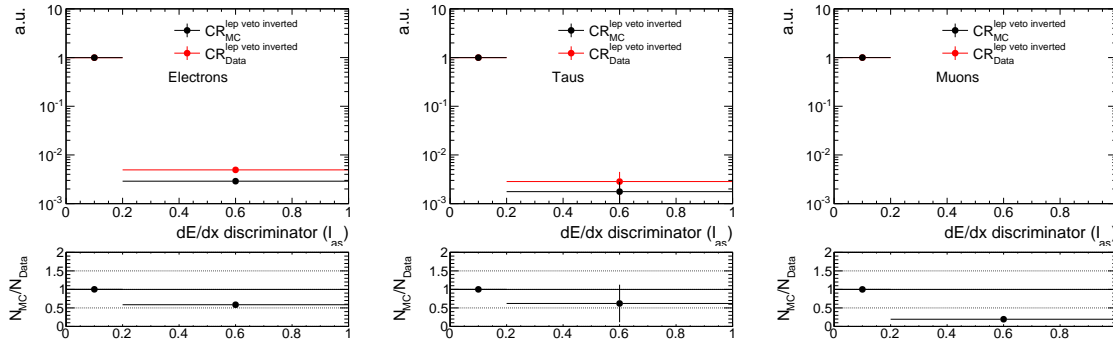


Figure 6.12: FIXME: be cleare about mc and data . Underlying histograms to estimate the leptonic I_{as} systematic uncertainty. Normalised distributions of the lepton I_{as} distributions in the lepton veto inverted control region for data (red) and simulation (black) for all three lepton types. The event-based selection requirements and the calorimeter isolation requirement are removed to enhance the statistical precision.

7 Optimisation of the search sensitivity

Finally, having all background estimation methods in place, an optimisation procedure is conducted to increase the search sensitivity with respect to the signal models introduced in Section 4.2. The optimisation is done in the most sensitive variables, p_T and I_{as} . In this optimisation, the full systematic uncertainty is taken into account, which includes statistical uncertainties arising from limited statistical precision of the samples used in the background estimation methods and the systematic uncertainties that are described in Section 6.4. In order to avoid unnecessary fine-tuning of the optimisation to the specific cross sections of the SUSY models and to keep the search as general as possible, the optimisation is not done by maximising $S/\Delta B$ but by minimising the cross section for which a 5σ discovery is possible

$$\frac{\sigma_{\min} \cdot \mathcal{L}}{\Delta B} = \frac{\sigma_{\min} \cdot \mathcal{L}}{\sqrt{\Delta B_{\text{stat}} + \Delta B_{\text{sys}}}} \geq 5. \quad (7.1)$$

In this formula, \mathcal{L} is the integrated luminosity in 2012, σ_{\min} is the cross section to be minimised, ΔB_{sys} is the systematic uncertainty of the background prediction as explained above and ΔB_{stat} is the statistical uncertainty of the background prediction which is the 68% one sided upper limit of a poisson distribution with $\mu = B$ estimated with the Neyman construction [15, 41].

Four different benchmark models are choosen for the optimisation. As this analysis focus on short tracks, models with charginos with low lifetimes are choosen: $c\tau = 1$ cm and $c\tau = 5$ cm. Additionally, two different masses in order to cover also the mass dimension: 100 GeV and 500 GeV.

A visualised optimisation is done by imposing general systematic uncertainties on the leptonic and the fake background of 100% and 20% respectively whereas the uncertainties arising from limited statistical precision of the samples are propagated accurately into the formula 7.1. The results can be found in Fig. 7.1, where the minimal cross section that is possible to exclude is shown in the $p_T - I_{as}$ plane. A exact optimisation taken the whole background uncertainties precisly into account is done without a visualisation. The corresponding results are shown in Table 7.1.

It can be seen that the optimal selections are highly dependent on the signal models.

Additionally, it is checked whether a sensitivity increase can be achieved by imposing also a selection on the number of missing outer hits N_{lost}^{outer} . For low lifetimes, a tiny increase in sensistivy is possible by selecting also in this variable but as this variable

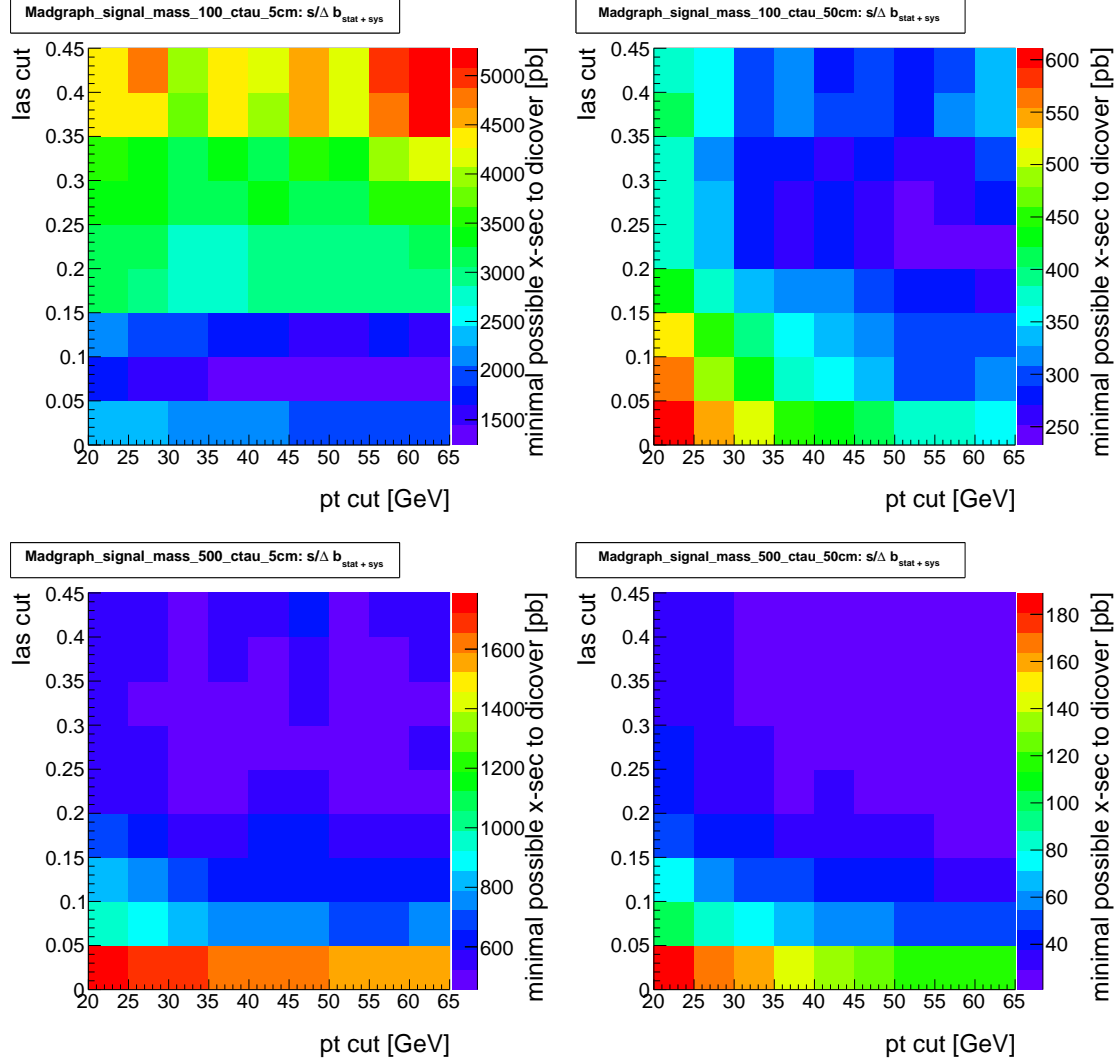


Figure 7.1: Minimal possible cross section to exclude in the $I_{as} - p_T$ plane for four different signal models. The systematic uncertainties are taken to be 20% and 100% for the fake and the leptonic background respectively. The uncertainty of the background arising from the limited size of datasets are propagated exactly to the search optimisation.

comes with new sources of uncertainties this is not considered in this search.

To have an optimal coverage over a wide mass space, four different signal regions are defined:

- 1.) $30 \text{ GeV} < p_T < 50 \text{ GeV}$ and $0.05 < I_{as} < 0.3$
- 2.) $30 \text{ GeV} < p_T < 50 \text{ GeV}$ and $I_{as} > 0.3$
- 3.) $p_T > 50 \text{ GeV}$ and $0.05 < I_{as} < 0.3$

Table 7.1: Optimal p_T and I_{as} cuts and corresponding minimal possible cross section σ_{\min} to exclude for different signal models.

Mass [GeV]	Lifetime [cm]	Optimal p_T cut	Optimal I_{as} cut	σ_{\min}
100	1	30	0.05	59.0291
500	1	0	0.0	10000.0000
100	5	50	0.05	2.6965
500	5	50	0.30	0.6180

4.) $p_T > 50 \text{ GeV}$ and $I_{as} > 0.3$.

8 Results

After the development of the background estimation methods for all different background sources and their corresponding systematic uncertainties (all explained in Section 6), the search is performed in four different signal regions with 19.7 fb^{-1} of data collected at a centre-of-mass energy of $\sqrt{s} = 8 \text{ TeV}$ at the CMS experiment. The comparison between the predicted number of events and the number of observed events is shown in Fig. 8.1. The corresponding numbers of predicted and observed events can be found in Table 8.1. The event yields observed in data after each selection requirement for the four signal regions are listed in Table ?? in Appendix ??.

The results are compatible in all four signal regions with the Standard Model background within the 1σ uncertainties. No excess above the SM prediction is in either of the four signal regions observed. That means, there is no evidence for physics beyond the Standard Model.

Therefore, in the following section the result is interpreted within the context of a supersymmetric model with a wino-like $\tilde{\chi}_1^\pm$ and $\tilde{\chi}_1^0$.

Table 8.1: Number of predicted and observed events for the four different signal regions.

Signal region	Prediction	Observation
$30 \text{ GeV} < p_T < 50 \text{ GeV}$ and $0.05 < I_{\text{as}} < 0.3$	0	0
$30 \text{ GeV} < p_T < 50 \text{ GeV}$ and $I_{\text{as}} > 0.3$	0	0
$p_T > 50 \text{ GeV}$ and $0.05 < I_{\text{as}} < 0.3$	0	0
$p_T > 50 \text{ GeV}$ and $I_{\text{as}} > 0.3$	0	0

9 Interpretation

In order to interpret the result of the search in the context of supersymmetric models with wino-like $\tilde{\chi}_1^\pm$ and $\tilde{\chi}_1^0$, the sources and sizes of uncertainties of the simulated signal

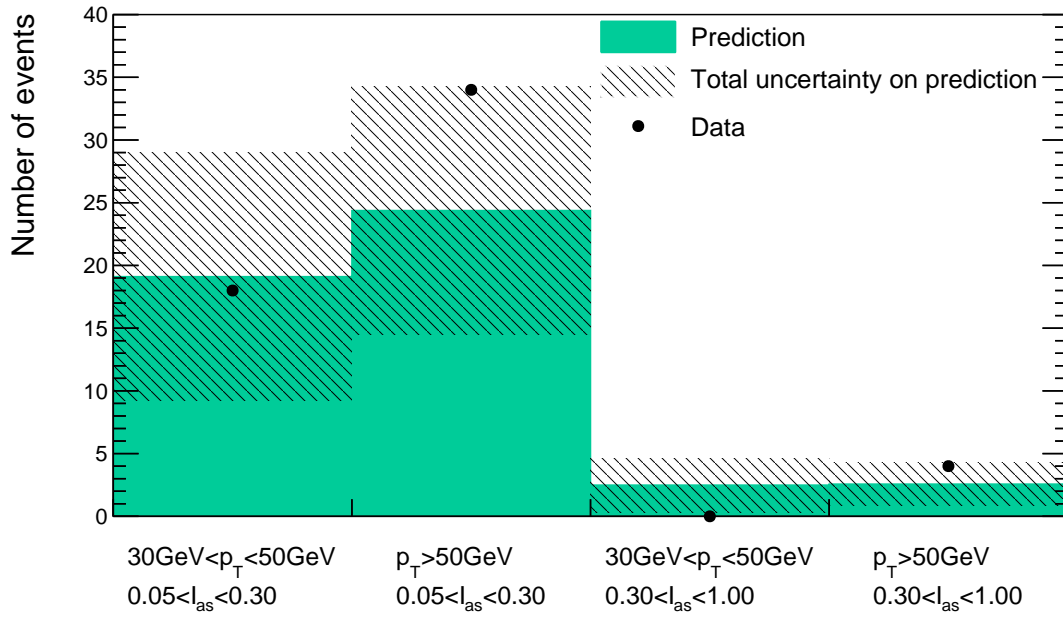


Figure 8.1: Number of predicted (green area) and observed (black dots) events for the four different signal regions. The hashed area represents the total uncertainty on the background prediction.

events must be estimated. Furthermore, the size of correlations between the systematic uncertainties must be determined to be able to combine the results of all four signal regions. The interpretation will then be done with statistical methods, that allow for the exclusion of parts of the supersymmetric parameter space on a 95% confidence level.

9.1 Systematic uncertainties of simulated signal samples

The systematic uncertainties on the number of signal events in the four signal regions are mainly caused by uncertainties on the quality of the simulation. This influences the signal efficiency of every selection requirements done in this analysis. Furthermore, an uncertainty on the overall number of events is caused by the uncertainty on the integrated luminosity recorded in 2012 at CMS and the theoretical signal cross-sections.

Luminosity uncertainty

The integrated luminosity recorded at CMS during the year 2012 is not exactly known. A detailed explanation of the so-called cluster counting method from the silicon pixel detector to measure the luminosity and the corresponding total uncertainty of 2.6% can be found in [42].

Uncertainty on the theoretical cross section

The theoretical cross section of $\tilde{\chi}_1^\pm \tilde{\chi}_1^\mp$ and $\tilde{\chi}_1^\pm \tilde{\chi}_1^0$ production at a centre-of-mass energy of 8 TeV are taken from [29, 30]. The corresponding theoretical uncertainties are ranging between 3 – 10%.

Uncertainty on the simulation of initial state radiation

Initial state radiation affects the transverse momentum distribution of the 2-particle system, $p_T (p_1^\mu + p_2^\mu)$, in a 2-body decay. Differences between data and simulation of ISR are taken into account by reweighting the transverse momentum of the $\tilde{\chi}_1^\pm \tilde{\chi}_1^\mp$ or $\tilde{\chi}_1^\pm \tilde{\chi}_1^0$ system. The weights are determined with a comparison of the simulated and observed p_T distribution of Z and $t\bar{t}$ events, done in [43]. To account for the systematic uncertainties on the reweighting procedure, the event weights are varied up and down dependent on the $p_T^{\chi_1\chi_2}$ up to variations of 25%. The resulting uncertainty on the ISR simulation is 10 – 13%.

Uncertainty on the simulation of the trigger efficiency

The HLTMonoCentralPFJet80_PFMETnoMu105_NHEF0p95 trigger with the higher MET threshold of 105 GeV active in Run C and Run D during 2012 was not available in the sim-

ulated signal samples. It is therefore emulated using L1 trigger information. More details on the emulation of this trigger can be found in Appendix ??.

The trigger uncertainty is accessed by comparing data-simulation differences of the trigger efficiency. This has been done within [31,32]. The resulting differences are applied as variations of the event weights of the simulated samples. The corresponding uncertainty lies between 2.6 – 4.6% for the signal samples.

Uncertainty on the jet energy scale

The transverse momentum of all jets is corrected for non-uniformities in the energy response as a function of the jet η and p_T [44] and for data-simulation differences. The uncertainty on the jet energy scale arise from the systematic uncertainty of the jet response in data like jet fragmentation, jet flavor composition, etc., neatly described in [44]. The correction is applied as a multiplicand on each jet's transverse momentum contained in an event. The corresponding systematic uncertainty is accessed by a up and down variation of the correction factor within 1σ . The resulting uncertainties are of minor importance and lie between 0.5 – 1.1%.

Uncertainty on the jet energy resolution

The jet energy resolution is smaller in simulation than in measured data (see Part ??). To take into account these differences, the jet energy response is additionnaly smeared to match the measured response. The systematic uncertainties cover the uncertainty on the resolution in data, like the jet energy scale uncertainty, uncertainties arising from non-Gaussian tails etc. [44,45]. The resulting uncertainty on the signal efficiency is between 0.1 – 0.7% and therefore almost negliglbe.

Uncertainty on the simulation of the parton distribution functions

The parton distribution function (PDF) used for the simulation of proton-proton collisions is provided by the CTEQ group [46] (see Section ?? for more information about PDFs). In [46], a detailed description of the methodology of the determination of a parton distribution function and its uncertainties is given. Pratically, the estimation of the PDF uncertainty is done by the application of 44 different sets of event weights which take into account 22 different sources of uncertainties [47,48] (up and down variations lead to a factor of 2). The sources correspond inter alia to uncertainties in the single distributions of gluons, up/down-quarks, etc, with the gluon distribution being by far the largest source of uncertainty.

The resulting uncertainties on the signal efficiency are between 3 – 5%.

Uncertainty of the pile-up distribution

As mentioned before, the distribution of the number of primary vertices is reweighted to match the measured distribution in data. The number of interactions in data on the other hand is determined by the luminosity of each bunch-crossing times the proton-proton inelastic cross section. The uncertainty on the number of interactions consists thus out of the uncertainty on the luminosity and the uncertainty on the cross section. This uncertainty is accessed by varying the inelastic cross section by plus/minus 5%.

The signal efficiency is only affected with less than 1% by this systematic uncertainty.

Uncertainty on the simulation of the calorimeter isolation

The uncertainty on the simulation of the calorimeter isolation $E_{\text{calo}}^{\Delta R < 0.5}$ is estimated by the comparison of the cut selection efficiency of $E_{\text{calo}}^{\Delta R < 0.5} < 5 \text{ GeV}$ in the fake enriched control sample $\text{CR}_{I_{\text{as}}}^{\text{fake}}$. The fake enriched control region is well suited for this estimation, as fake tracks are also expected to deposit only a low amount of energy in the calorimeters. The selection efficiency in data is higher than in simulation in both p_{T} bins of $30 - 50 \text{ GeV}$ and $50 - \infty \text{ GeV}$, which results in an uncertainty of 12% and 3% respectively.

Uncertainty on the simulation of missing middle/inner hits

The uncertainty on the simulation of the number of missing inner and middle hits is assessed by comparing the probability of passing the selection requirements of $N_{\text{miss}}^{\text{middle/inner}} = 0$ of a candidate track in the muon-veto inverted control region. This control region is particularly suitable because muons are neither expected to have intrinsic sources of missing hits, as pions or electrons have. Pions can interact nuclearly with the tracker material and electrons can have sizeable radiative losses, such that both can change direction or don't deposit energy in a tracker layer. For muons, on the other hand, sources of missing inner and middle hits are mainly algorithmical [31, 32], making them very similar to the algorithmic sources of missing inner/middle hits for chargino tracks.

The uncertainty is estimated as the relative difference of the cut selection efficiency of $N_{\text{miss}}^{\text{middle/inner}} = 0$ in data and simulation. The selection efficiency is always higher in simulation, resulting in systematic uncertainties of around 3.5% for the simulation of $N_{\text{miss}}^{\text{inner}} = 0$ and around 2.0% for $N_{\text{miss}}^{\text{middle}} = 0$. The uncertainties are of very similar size in the signal regions with different p_{T} . No I_{as} dependence is considered.

Uncertainty on the simulation of the I_{as}

FIXME

Uncertainty on the simulation of the track reconstruction efficiency

One final source of uncertainty is the simulation of the track reconstruction efficiency. Possible differences of the reconstruction efficiency in simulation and data can lead to a different signal acceptance. Differences in the track reconstruction efficiency are especially expected for short tracks. Therefore, a worst case estimation is done, comparing the track reconstruction efficiency in data and simulation for tracks with a number of hits of three.

In simulation and observed data, well reconstructed muon tracks are selected and all hits after the third hits are removed. Afterwards the full track reconstruction step is again preformed. The relative difference of the track efficiency in data and simulation ($\epsilon = N_{\text{recon. track with } N_{\text{hits}}=3} / N_{\text{selected muon trks}}$) is taken as systematic uncertainty. The track reconstruction efficiency is higher in simulation than in data and results in uncertainties between 4.5 – 6.0%.

9.2 Correlation of systematic uncertainties

In order to combine the four different signal regions, a specification of the size of correlations between the systematic uncertay needs to be addresses.

Background correlations

Signal correlation

9.3 Statistical Methods/ Limit setting

Finally, bla bla bla.

9.4 Exclusion limits

- 1-d limits
- 2-d limits

10 Discussion and outlook and conclusion

A Detailed event yield tables for simulated samples and data

Table A.1: Event yields after each selection step for various background processes. FIXME
update this table with correct ttjets sample!!

Selection	$W + \text{jets}$	$t\bar{t} + \text{jets}$	$Z \rightarrow \ell\bar{\ell}$	Multijet
after skim ($p_{\text{T}}^{\text{1,jets}} > 60 \text{ GeV}$)	$9.16 \cdot 10^7$	$1.04 \cdot 10^6$	$2.21 \cdot 10^7$	$1.38 \cdot 10^{11}$
trigger	$4.31 \cdot 10^6$	$1.12 \cdot 10^5$	$4.23 \cdot 10^3$	$4.32 \cdot 10^6$
$p_{\text{T}}^{\text{1,jet}} > 100 \text{ GeV}$	$3.07 \cdot 10^6$	$7.89 \cdot 10^4$	$1.02 \cdot 10^3$	$1.15 \cdot 10^6$
$\cancel{E}_{\text{T}} > 100 \text{ GeV}$	$1.89 \cdot 10^6$	$5.17 \cdot 10^4$	$6.26 \cdot 10^2$	$9.63 \cdot 10^5$
$\Delta\phi_{\text{max}}(\text{jet}_i, \text{jet}_j) < 2.7$	$1.11 \cdot 10^6$	$6.58 \cdot 10^3$	$1.32 \cdot 10^2$	$9.55 \cdot 10^3$
$\Delta\phi_{\text{max}}(\text{jet}_i, \cancel{E}_{\text{T}}) > 0.5$	$1.11 \cdot 10^6$	$6.64 \cdot 10^3$	$1.32 \cdot 10^2$	$2.01 \cdot 10^4$
≥ 1 reconstructed trk	$1.10 \cdot 10^6$	$6.57 \cdot 10^3$	$1.32 \cdot 10^2$	$9.55 \cdot 10^3$
≥ 1 high-purity trk	$1.10 \cdot 10^6$	$6.57 \cdot 10^3$	$1.32 \cdot 10^2$	$9.55 \cdot 10^3$
≥ 1 trk with $N_{\text{miss}}^{\text{middle}} = 0$	$1.09 \cdot 10^6$	$6.55 \cdot 10^3$	$1.32 \cdot 10^2$	$9.55 \cdot 10^3$
≥ 1 trk with $N_{\text{miss}}^{\text{inner}} = 0$	$1.07 \cdot 10^6$	$6.53 \cdot 10^3$	$1.32 \cdot 10^2$	$9.55 \cdot 10^3$
≥ 1 trk with $ d0 < 0.02 \text{ cm}$	$1.07 \cdot 10^6$	$6.47 \cdot 10^3$	$1.32 \cdot 10^2$	$9.55 \cdot 10^3$
≥ 1 trk with $ dz < 0.5 \text{ cm}$	$1.07 \cdot 10^6$	$6.46 \cdot 10^3$	$1.32 \cdot 10^2$	$9.55 \cdot 10^3$
≥ 1 trk with $ \eta < 2.1$	$1.03 \cdot 10^6$	$6.41 \cdot 10^3$	$1.32 \cdot 10^2$	$9.55 \cdot 10^3$
≥ 1 trk with $p_{\text{T}} > 10 \text{ GeV}$	$1.03 \cdot 10^6$	$6.41 \cdot 10^3$	$1.32 \cdot 10^2$	$9.55 \cdot 10^3$
≥ 1 trk without a μ within $\Delta R < 0.15$	$9.85 \cdot 10^5$	$6.32 \cdot 10^3$	$1.14 \cdot 10^2$	$9.55 \cdot 10^3$
≥ 1 trk without an e within $\Delta R < 0.15$	$9.55 \cdot 10^5$	$6.22 \cdot 10^3$	$8.53 \cdot 10^1$	$9.55 \cdot 10^3$
≥ 1 trk without a τ within $\Delta R < 0.15$	$9.53 \cdot 10^5$	$6.21 \cdot 10^3$	$8.53 \cdot 10^1$	$9.55 \cdot 10^3$
≥ 1 trk without a jet within $\Delta R < 0.5$	$9.15 \cdot 10^5$	$6.13 \cdot 10^3$	$8.53 \cdot 10^1$	$9.55 \cdot 10^3$
≥ 1 trk ! within $\Delta R < 0.05$ of a dead/noisy ECAL cell	$3.70 \cdot 10^5$	$3.78 \cdot 10^3$	$8.53 \cdot 10^1$	$0.00 \cdot 10^0$
≥ 1 trk ! within an ECAL intermodule gap	$3.52 \cdot 10^5$	$3.61 \cdot 10^3$	$8.53 \cdot 10^1$	$0.00 \cdot 10^0$
≥ 1 trk ! within $1.42 < \eta < 1.65$	$2.21 \cdot 10^5$	$2.30 \cdot 10^3$	$0.00 \cdot 10^0$	$0.00 \cdot 10^0$
≥ 1 trk ! within $\Delta R < 0.25$ to a bad CSC	$1.04 \cdot 10^4$	$1.20 \cdot 10^2$	$0.00 \cdot 10^0$	$0.00 \cdot 10^0$
≥ 1 trk with $\sum_{\Delta R < 0.3} p_{\text{T}}/p_{\text{T}}^{\text{cand}} < 0.1$	$8.14 \cdot 10^3$	$7.96 \cdot 10^1$	$0.00 \cdot 10^0$	$0.00 \cdot 10^0$

Table A.2: Event yields after each selection step for various signal models. FIXME update this table with other signal samples!!

Selection	m=100 GeV $c\tau=10$ cm	m=100 GeV $c\tau=100$ cm	m=500 GeV $c\tau=10$ cm	m=500 GeV $c\tau=100$ cm
before selection	$3.41 \cdot 10^5$	$3.41 \cdot 10^5$	$3.46 \cdot 10^2$	$3.46 \cdot 10^2$
trigger	$1.56 \cdot 10^4$	$1.49 \cdot 10^4$	$4.63 \cdot 10^1$	$4.61 \cdot 10^1$
$p_T^{1.\text{jet}} > 100$ GeV	$1.10 \cdot 10^4$	$1.05 \cdot 10^4$	$3.65 \cdot 10^1$	$3.58 \cdot 10^1$
$\cancel{E}_T > 100$ GeV	$1.09 \cdot 10^4$	$9.84 \cdot 10^3$	$3.63 \cdot 10^1$	$3.56 \cdot 10^1$
$\Delta\phi_{\text{max}}(\text{jet}_i, \text{jet}_j) < 2.7$	$7.91 \cdot 10^3$	$6.99 \cdot 10^3$	$2.76 \cdot 10^1$	$2.70 \cdot 10^1$
$\Delta\phi_{\text{max}}(\text{jet}_i, \cancel{E}_T) > 0.5$	$7.91 \cdot 10^3$	$7.04 \cdot 10^3$	$2.77 \cdot 10^1$	$2.71 \cdot 10^1$
≥ 1 reconstructed trk	$3.13 \cdot 10^3$	$5.75 \cdot 10^3$	$5.74 \cdot 10^0$	$2.13 \cdot 10^1$
≥ 1 high-purity trk	$2.91 \cdot 10^3$	$5.66 \cdot 10^3$	$5.25 \cdot 10^0$	$2.08 \cdot 10^1$
≥ 1 trk with $N_{\text{miss}}^{\text{middle}} = 0$	$2.87 \cdot 10^3$	$5.46 \cdot 10^3$	$5.23 \cdot 10^0$	$2.02 \cdot 10^1$
≥ 1 trk with $N_{\text{miss}}^{\text{inner}} = 0$	$2.86 \cdot 10^3$	$5.41 \cdot 10^3$	$5.22 \cdot 10^0$	$2.01 \cdot 10^1$
≥ 1 trk with $ d0 < 0.02$ cm	$2.81 \cdot 10^3$	$5.39 \cdot 10^3$	$5.08 \cdot 10^0$	$1.99 \cdot 10^1$
≥ 1 trk with $ dz < 0.5$ cm	$2.80 \cdot 10^3$	$5.39 \cdot 10^3$	$5.08 \cdot 10^0$	$1.99 \cdot 10^1$
≥ 1 trk with $ \eta < 2.1$	$2.63 \cdot 10^3$	$4.98 \cdot 10^3$	$5.01 \cdot 10^0$	$1.91 \cdot 10^1$
≥ 1 trk with $p_T > 10$ GeV	$2.63 \cdot 10^3$	$4.98 \cdot 10^3$	$5.01 \cdot 10^0$	$1.91 \cdot 10^1$
≥ 1 trk without a μ within $\Delta R < 0.15$	$2.63 \cdot 10^3$	$4.70 \cdot 10^3$	$5.01 \cdot 10^0$	$1.89 \cdot 10^1$
≥ 1 trk without an e within $\Delta R < 0.15$	$2.63 \cdot 10^3$	$4.70 \cdot 10^3$	$5.01 \cdot 10^0$	$1.89 \cdot 10^1$
≥ 1 trk without a τ within $\Delta R < 0.15$	$2.63 \cdot 10^3$	$4.68 \cdot 10^3$	$5.01 \cdot 10^0$	$1.89 \cdot 10^1$
≥ 1 trk without a jet within $\Delta R < 0.5$	$2.61 \cdot 10^3$	$4.64 \cdot 10^3$	$4.89 \cdot 10^0$	$1.84 \cdot 10^1$
≥ 1 trk !within $\Delta R < 0.05$ of a dead/noisy ECAL cell	$2.40 \cdot 10^3$	$4.30 \cdot 10^3$	$4.44 \cdot 10^0$	$1.71 \cdot 10^1$
≥ 1 trk !within an ECAL intermodule gap	$2.38 \cdot 10^3$	$4.27 \cdot 10^3$	$4.41 \cdot 10^0$	$1.70 \cdot 10^1$
≥ 1 trk !within $1.42 < \eta < 1.65$	$2.16 \cdot 10^3$	$3.92 \cdot 10^3$	$4.19 \cdot 10^0$	$1.58 \cdot 10^1$
≥ 1 trk !within $\Delta R < 0.25$ to a bad CSC	$2.06 \cdot 10^3$	$3.71 \cdot 10^3$	$4.06 \cdot 10^0$	$1.52 \cdot 10^1$
≥ 1 trk with $\sum_{\Delta R < 0.3} p_T/p_T^{\text{cand}} < 0.1$	$2.03 \cdot 10^3$	$3.67 \cdot 10^3$	$4.00 \cdot 10^0$	$1.51 \cdot 10^1$

B Selection requirements of the “tag-and-probe” samples

Table B.1: Event selection cuts for the muon “tag-and-probe” sample that is used to estimate the uncertainty on the muon scale factor ρ_{MC}^μ .

Muon selection	$p_{\text{T}} > 25 \text{ GeV}$ $ \eta < 2.4$ $\sum_{\Delta R < 0.4} p_{\text{T}}^{\text{PF particle}} / p_{\text{T}}(\mu) < 0.12$ $\frac{\chi^2}{ndof} \Big _{\text{global track}} < 10$ $ d0 < 0.2 \text{ cm}$ $ dz < 0.5 \text{ cm}$ ≥ 1 hit in the muon detector ≥ 2 hits in different muon detector planes ≥ 1 hit in the pixel detector ≥ 6 hits in the tracker system
Candidate track selection	Good quality selection Kinematic selection Lepton/jet veto Isolation selection $N_{\text{hits}} > 5$
Event-based selection	Muon and candidate track opposite in charge $80 \text{ GeV} < M_{\text{inv}}(\mu, \text{can. trk}) < 100 \text{ GeV}$

Table B.2: Event selection cuts for the tau “tag-and-probe” sample that is used to estimate the uncertainty on the tau scale factor ρ_{MC}^τ .

Muon selection that is compatible with a $\tau \rightarrow \mu\nu\nu$ decay	$p_{\text{T}} > 25 \text{ GeV}$ $ \eta < 2.4$ $\sum_{\Delta R < 0.4} p_{\text{T}}^{\text{PF particle}} / p_{\text{T}}(\mu) < 0.12$ $\left. \frac{\chi^2}{ndof} \right _{\text{global track}} < 10$ $ d0 < 0.2 \text{ cm}$ $ dz < 0.5 \text{ cm}$ ≥ 1 hit in the muon detector ≥ 2 hits in different muon detector planes ≥ 1 hit in the pixel detector ≥ 6 hits in the tracker system
Candidate track selection	Good quality selection Kinematic selection Lepton/jet veto $\sum_{\Delta R < 0.3} p_{\text{T}} / p_{\text{T}}^{\text{cand}} < 0.1$ $N_{\text{hits}} > 5$
Event-based selection	Muon and candidate track opposite in charge $40 \text{ GeV} < M_{\text{inv}}(\mu, \text{cand. trk}) < 75 \text{ GeV}$ $m_{\text{T}}(\mu, \cancel{E}_{\text{T}}) < 40 \text{ GeV}$

Table B.3: Event selection cuts for the electron “tag-and-probe” sample that is used to estimate the uncertainty on the electron scale factor ρ_{MC}^e .

Electron selection	$p_{\text{T}} > 25 \text{ GeV}$ $ \eta < 2.5$ $\sum_{\Delta R < 0.4} p_{\text{T}}^{\text{PF particle}} / p_{\text{T}}(e) < 0.15$ pass conversion veto no missing tracker hits good MVA electron as defined in [37]
Candidate track selection	Good quality selection Kinematic selection Lepton/jet veto $\sum_{\Delta R < 0.3} p_{\text{T}} / p_{\text{T}}^{\text{cand}} < 0.1$ $N_{\text{hits}} > 5$
Event-based selection	Electron and candidate track opposite in charge $80 \text{ GeV} < M_{\text{inv}}(e, \text{cand. trk}) < 100 \text{ GeV}$

C Validation tests of the background estimation methods

Table C.1: Validation tests of the background estimation methods in the calorimeter isolation control region $E_{\text{calo}}^{\Delta R < 0.5} > 10 \text{ GeV}$ for two different p_{T} selection requirements: $p_{\text{T}} > 40 \text{ GeV}$ (left) and $p_{\text{T}} > 60 \text{ GeV}$ (right). Only statistical uncertainties are included.

	Predicted Yield	Data Yield		Predicted Yield	Data Yield
Total bkg	$84.36^{+16.47}_{-10.88}$	94	Total bkg	$35.56^{+11.95}_{-6.20}$	53
Electrons	$15.69^{+11.92}_{-6.72}$		Electrons	$0.00^{+9.14}_{-0.00}$	
Muons	$5.67^{+7.74}_{-3.55}$		Muons	$3.65^{+4.98}_{-2.28}$	
Taus	$35.78^{+5.09}_{-4.18}$		Taus	$13.22^{+1.88}_{-1.55}$	
Fakes	$27.23^{+6.57}_{-6.57}$		Fakes	$18.70^{+5.55}_{-5.55}$	

Table C.2: Validation tests of the background estimation methods in the calorimeter isolation control region $E_{\text{calo}}^{\Delta R < 0.5} > 10 \text{ GeV}$ with an additional I_{as} selection of $I_{\text{as}} > 0.2$ for two different p_{T} selection requirements: $p_{\text{T}} > 40 \text{ GeV}$ (left) and $p_{\text{T}} > 60 \text{ GeV}$ (right). Only statistical uncertainties are included.

	Predicted Yield	Data Yield		Predicted Yield	Data Yield
Total bkg	$4.76^{+1.42}_{-1.39}$	8	Total bkg	$2.31^{+0.97}_{-0.95}$	3
Electrons	$0.20^{+0.17}_{-0.10}$		Electrons	$0.00^{+0.11}_{-0.00}$	
Muons	$0.00^{+0.22}_{-0.00}$		Muons	$0.00^{+0.14}_{-0.00}$	
Taus	$0.48^{+0.15}_{-0.11}$		Taus	$0.18^{+0.06}_{-0.04}$	
Fakes	$4.08^{+1.38}_{-1.38}$		Fakes	$2.14^{+0.95}_{-0.95}$	

Table C.3: Validation tests of the background estimation methods in the calorimeter isolation control region $E_{\text{calo}}^{\Delta R < 0.5} > 10 \text{ GeV}$ with an additional I_{as} selection of $I_{\text{as}} > 0.4$ for two different p_{T} selection requirements: $p_{\text{T}} > 40 \text{ GeV}$ (left) and $p_{\text{T}} > 60 \text{ GeV}$ (right). Only statistical uncertainties are included.

	Predicted Yield	Data Yield		Predicted Yield	Data Yield
Total bkg	$1.98^{+0.87}_{-0.83}$	2	Total bkg	$1.10^{+0.63}_{-0.61}$	1
Electrons	$0.00^{+0.05}_{-0.00}$		Electrons	$0.00^{+0.00}_{-0.00}$	
Muons	$0.00^{+0.22}_{-0.00}$		Muons	$0.00^{+0.14}_{-0.00}$	
Taus	$0.08^{+0.09}_{-0.04}$		Taus	$0.03^{+0.03}_{-0.02}$	
Fakes	$1.91^{+0.83}_{-0.83}$		Fakes	$1.07^{+0.61}_{-0.61}$	

The underprediction in the control regions with $I_{\text{as}} > 0.2$ is caused by the prediction of the leptonic I_{as} shape from simulation. This leads to a bias as the I_{as} distribution in simulation is softer than in data. However, this bias is taken into account as systematic uncertainty (see Section 6.4.4).

Bibliography

- [1] CMS Collaboration, “Search for new physics in the multijet and missing transverse momentum final state in proton-proton collisions at $\sqrt{s}=8$ TeV”, *JHEP* **06** (2014) 055, [arXiv:1402.4770](#). doi:10.1007/JHEP06(2014)055.
- [2] CMS Collaboration, “Searches for Supersymmetry using the M_{T2} Variable in Hadronic Events Produced in pp Collisions at 8 TeV”, *JHEP* **05** (2015) 078, [arXiv:1502.04358](#). doi:10.1007/JHEP05(2015)078.
- [3] ATLAS Collaboration, “Search for squarks and gluinos with the ATLAS detector in final states with jets and missing transverse momentum using $\sqrt{s}=8$ TeV proton-proton collision data”, *JHEP* **09** (2014) 176, [arXiv:1405.7875](#). doi:10.1007/JHEP09(2014)176.
- [4] M. Ibe, S. Matsumoto, S. Shirai et al., “Wino Dark Matter in light of the AMS-02 2015 Data”, *Phys. Rev.* **D91** (2015), no. 11, 111701, [arXiv:1504.05554](#). doi:10.1103/PhysRevD.91.111701.
- [5] T. Moroi, M. Nagai, and M. Takimoto, “Non-Thermal Production of Wino Dark Matter via the Decay of Long-Lived Particles”, *JHEP* **07** (2013) 066, [arXiv:1303.0948](#). doi:10.1007/JHEP07(2013)066.
- [6] CMS Collaboration, “Search for disappearing tracks in proton-proton collisions at $\sqrt{s}=8$ TeV”, *JHEP* **01** (2015) 096, [arXiv:1411.6006](#). doi:10.1007/JHEP01(2015)096.
- [7] CMS Collaboration, “Searches for long-lived charged particles in pp collisions at $\sqrt{s}=7$ and 8 TeV”, *JHEP* **07** (2013) 122, [arXiv:1305.0491](#). doi:10.1007/JHEP07(2013)122.
- [8] CMS Collaboration, “Phenomenological MSSM interpretation of the CMS 2011 5fb-1 results”, *CMS Physics Analysis Summary* **CMS-PAS-SUS-12-030** (2013).
- [9] CMS Collaboration, “Reinterpreting the results of the search for long-lived charged particles in the pMSSM and other BSM scenarios”, *CMS Physics Analysis Summary* **CMS-PAS-EXO-13-006** (2014).

- [10] CMS Collaboration, “Search for disappearing tracks in proton-proton collisions at $\sqrt{s} = 8$ TeV”, *Public CMS Wiki* (2015).
<https://twiki.cern.ch/twiki/bin/view/CMSPublic/PhysicsResultsEXO12034>, Topic revision: r9.
- [11] CMS Collaboration, “Search for heavy long-lived charged particles in pp collisions at $\sqrt{s} = 7$ TeV”, *Phys. Lett.* **B713** (2012) 408–433, [arXiv:1205.0272](#).
[doi:10.1016/j.physletb.2012.06.023](#).
- [12] CMS Collaboration, “Description and performance of track and primary-vertex reconstruction with the CMS tracker”, *JINST* **9** (2014), no. 10, P10009,
[arXiv:1405.6569](#). [doi:10.1088/1748-0221/9/10/P10009](#).
- [13] H. Bethe, “Theory of the Passage of Fast Corpuscular Rays Through Matter”,
Annalen Phys. **5** (1930) 325–400. [*Annalen Phys.* 397,325(1930)].
[doi:10.1002/andp.19303970303](#).
- [14] “National Institute of Standards and Technology”.
<http://physics.nist.gov/cgi-bin/Star/compos.pl?mode=text&matno=014>.
Accessed: 2015-10-21.
- [15] Particle Data Group Collaboration, “Review of Particle Physics”, *Chin. Phys.* **C38**
(2014) 090001. [doi:10.1088/1674-1137/38/9/090001](#).
- [16] L. Landau, “On the energy loss of fast particles by ionization”, *J. Phys.(USSR)* **8**
(1944) 201–205.
- [17] H. Bichsel, “Straggling in Thin Silicon Detectors”, *Rev. Mod. Phys.* **60** (1988)
663–699. [doi:10.1103/RevModPhys.60.663](#).
- [18] L. Quertenmont, “Search for Heavy Stable Charged Particles with the CMS
detector at the LHC”. PhD thesis, Louvain, U., 2010.
- [19] D. Kotlinski. personal communication.
- [20] T. W. Anderson, “On the Distribution of the Two-Sample Cramr-von Mises
Criterion”, *The Annals of Mathematical Statistics* **33** (1962), no. 3, pp. 1148–1159.
- [21] F. James, “Statistical methods in experimental physics”. 2006.
- [22] CMS Collaboration, “Tracking and Vertexing Results from First Collisions”, *CMS
Physics Analysis Summary CMS-PAS-TRK-10-001* (2010).
- [23] R. Gavin et al., “FEWZ 3.1: A User’s Guide”.
http://www.hep.anl.gov/fpetriello/FEWZManual_3.1.pdf. Accessed:
2015-10-27.

- [24] M. Czakon, P. Fiedler, and A. Mitov, “Total Top-Quark Pair-Production Cross Section at Hadron Colliders Through $O(\frac{4}{s})$ ”, *Phys. Rev. Lett.* **110** (2013) 252004, [arXiv:1303.6254](#). doi:10.1103/PhysRevLett.110.252004.
- [25] J. Alwall, R. Frederix, S. Frixione et al., “The automated computation of tree-level and next-to-leading order differential cross sections, and their matching to parton shower simulations”, *JHEP* **07** (2014) 079, [arXiv:1405.0301](#). doi:10.1007/JHEP07(2014)079.
- [26] T. Sjostrand, S. Mrenna, and P. Z. Skands, “PYTHIA 6.4 Physics and Manual”, *JHEP* **05** (2006) 026, [arXiv:hep-ph/0603175](#). doi:10.1088/1126-6708/2006/05/026.
- [27] GEANT4 Collaboration, “GEANT4: A Simulation toolkit”, *Nucl. Instrum. Meth.* **A506** (2003) 250–303. doi:10.1016/S0168-9002(03)01368-8.
- [28] J. Allison et al., “Geant4 developments and applications”, *IEEE Trans. Nucl. Sci.* **53** (2006) 270. doi:10.1109/TNS.2006.869826.
- [29] B. Fuks, M. Klasen, D. R. Lamprea et al., “Gaugino production in proton-proton collisions at a center-of-mass energy of 8 TeV”, *JHEP* **1210** (2012) 081, [arXiv:1207.2159](#). doi:10.1007/JHEP10(2012)081.
- [30] B. Fuks, M. Klasen, D. R. Lamprea et al., “Precision predictions for electroweak superpartner production at hadron colliders with Resummino”, *Eur.Phys.J.* **C73** (2013) 2480, [arXiv:1304.0790](#). doi:10.1140/epjc/s10052-013-2480-0.
- [31] J. D. Brinson, “A search for disappearing tracks in proton-proton collisions at $\sqrt{s} = 8$ TeV”. PhD thesis, Ohio State U.
- [32] C. H. J. Brinson and W. Wulsin, “Search for disappearing tracks”, *CMS Analysis Note* **CMS-AN-12-400** (2014). Internal documentation.
- [33] CMS Collaboration, “Tracking and Primary Vertex Results in First 7 TeV Collisions”, *CMS Physics Analysis Summary* **CMS-PAS-TRK-10-005** (2010).
- [34] A. B. et. al., “Search for New Physics in the Monojet final state at CMS”, *CMS Analysis Note* **CMS-AN-12-421** (2012). Internal documentation.
- [35] CMS Collaboration, “Search for dark matter, extra dimensions, and unparticles in monojet events in protonproton collisions at $\sqrt{s} = 8$ TeV”, *Eur. Phys. J.* **C75** (2015), no. 5, 235, [arXiv:1408.3583](#). doi:10.1140/epjc/s10052-015-3451-4.
- [36] CMS Collaboration, “Studies of Tracker Material”, *CMS Physics Analysis Summary* **CMS-PAS-TRK-10-003** (2010).

- [37] CMS Collaboration, “Measurement of Higgs boson production and properties in the WW decay channel with leptonic final states”, *JHEP* **01** (2014) 096, [arXiv:1312.1129](#). doi:10.1007/JHEP01(2014)096.
- [38] CMS Collaboration, “Performance of Electron Reconstruction and Selection with the CMS Detector in Proton-Proton Collisions at $s = 8$ TeV”, *JINST* **10** (2015), no. 06, P06005, [arXiv:1502.02701](#). doi:10.1088/1748-0221/10/06/P06005.
- [39] CMS Collaboration, “Performance of CMS muon reconstruction in pp collision events at $\sqrt{s} = 7$ TeV”, *JINST* **7** (2012) P10002, [arXiv:1206.4071](#). doi:10.1088/1748-0221/7/10/P10002.
- [40] CMS Collaboration, “Performance of tau-lepton reconstruction and identification in CMS”, *JINST* **7** (2012) P01001, [arXiv:1109.6034](#). doi:10.1088/1748-0221/7/01/P01001.
- [41] J. Neyman *Phil. Trans. Royal Soc. London, Series A* **236** (1937) 333–80. Reprinted in *A Selection of Early Statistical Papers on J. Neyman* (University of California Press, Berkeley, 1967).
- [42] CMS Collaboration, “CMS Luminosity Based on Pixel Cluster Counting - Summer 2013 Update”, *CMS Physics Analysis Summary CMS-PAS-LUM-13-001* (2013).
- [43] D. B. et. al., “Hadronic Recoil Studies of Heavy Boosted Systems”, *CMS Analysis Note CMS-AN-13-059* (2013). Internal documentation.
- [44] CMS Collaboration, “Jet Energy Scale and Resolution in the CMS Experiment”, *CMS Physics Analysis Summary CMS-PAS-JME-13-004* (2015).
- [45] K. Goebel, “Probing supersymmetry based on precise jet measurements at the CMS experiment”. PhD thesis, U. Hamburg, Dept. Phys., 2015.
- [46] J. Pumplin, D. R. Stump, J. Huston et al., “New generation of parton distributions with uncertainties from global QCD analysis”, *JHEP* **07** (2002) 012, [arXiv:hep-ph/0201195](#). doi:10.1088/1126-6708/2002/07/012.
- [47] M. Botje et al., “The PDF4LHC Working Group Interim Recommendations”, [arXiv:1101.0538](#).
- [48] A. Vicini, “Practical implementation of the PDF4LHC recipe”. http://www.hep.ucl.ac.uk/pdf4lh/PDF4LHC_practical_guide.pdf. Accessed: 2015-11-27.

